iScience

CellPress
OPEN ACCESS

Article

Communication subspace dynamics of the canonical olfactory pathway

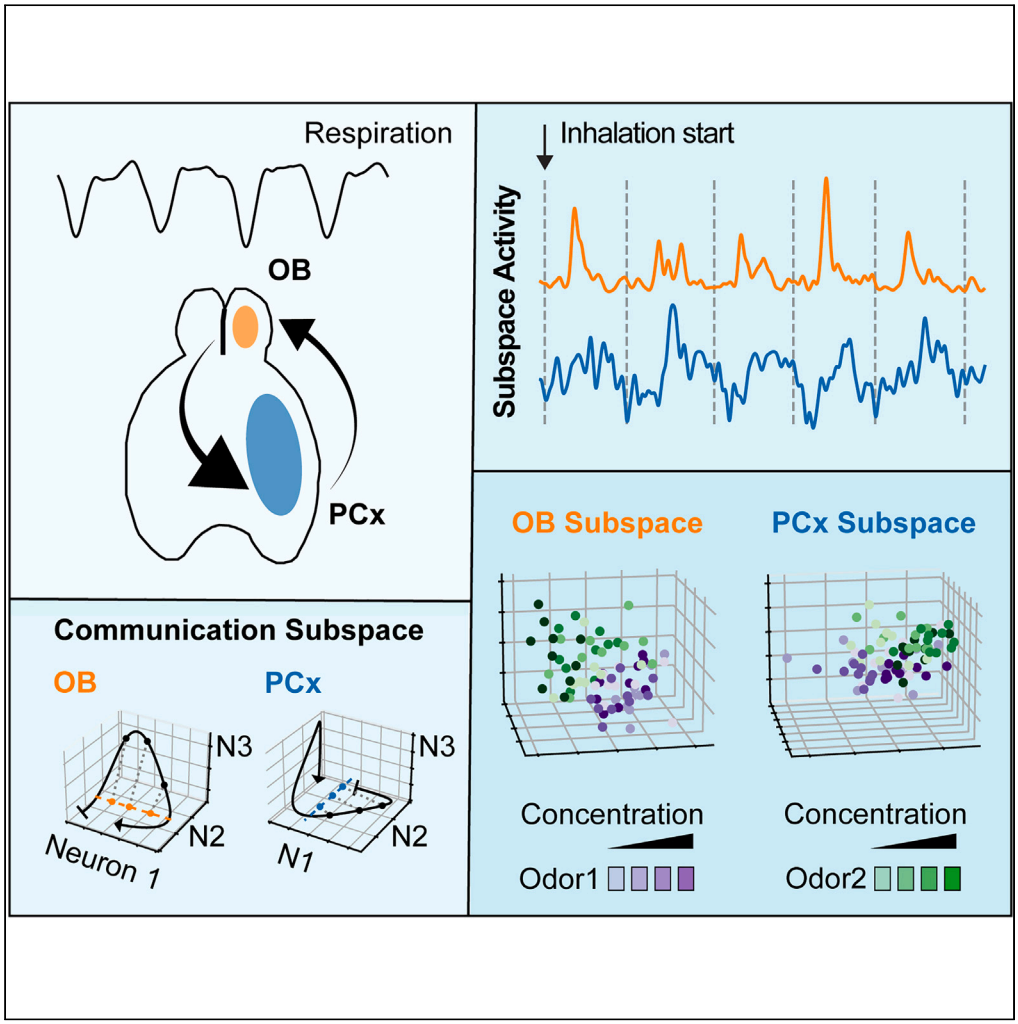

Joaquín Gonzalez, Pablo Torterolo, Kevin A. Bolding, Adriano B.L. Tort

joaqgonzar@gmail.com (J.G.)
tort@neuro.ufrn.br (A.B.L.T.)

Highlights

Neural populations in the olfactory system interact through a communication subspace

Breathing drives subspace activity and parses feedforward and feedback transmission

Communication depends causally on olfactory bulb and local piriform cortex activity

The olfactory communication subspace transmits a low-dimensional odor representation

Gonzalez et al., iScience 27, 111275
December 20, 2024
https://doi.org/10.1016/j.isci.2024.111275

iScience

CellPress
OPEN ACCESS

Article

Communication subspace dynamics of the canonical olfactory pathway

Joaquín Gonzalez,[1,2,4,*] Pablo Torterolo,[1] Kevin A. Bolding,[3] and Adriano B.L. Tort[2,*]

SUMMARY

Understanding how different brain areas communicate is crucial for elucidating the mechanisms underlying cognition. A possible way for neural populations to interact is through a communication subspace, a specific region in the state-space enabling the transmission of behaviorally relevant spiking patterns. In the olfactory system, it remains unclear if different populations employ such a mechanism. Our study reveals that neuronal ensembles in the main olfactory pathway (olfactory bulb to olfactory cortex) interact through a communication subspace, which is driven by nasal respiration and allows feedforward and feedback transmission to occur segregated along the sniffing cycle. Moreover, our results demonstrate that subspace communication depends causally on the activity of both areas, is hindered during anesthesia, and transmits a low-dimensional representation of odor.

INTRODUCTION

Understanding how different brain areas communicate is a central problem in neuroscience.[1,2] Large-scale cortical connections allow information to be integrated, a process fundamental for sensory perception, decision-making, and cognition.[3] Despite interregional communication being the basis of brain function, major problems challenge its study. At the circuit scale, communication relies on synapses formed by large populations of neurons from different areas, where the number of synapses far exceeds the number of neurons.[4] Moreover, cross-area interactions in the mammalian cortex can be feedforward, feedback, or bidirectional[5–8] and often comprise both excitatory and inhibitory connections.

To understand how brain areas communicate, we need to explain how the neuronal populations in each site interact to allow the transmission of behaviorally relevant spiking patterns.[9,10] In the neocortex, different areas can interact through a communication subspace,[11–18] a specific region in the state-space (where each dimension corresponds to the activity of a single neuron) of a local population that enables communication. In simpler words, communication occurs through local co-activity patterns that maximize the correlation between two areas. This idea implies that all of the variance and information embedded in the activity of a neural population is not equally transmitted to connected brain regions. Rather, there are specific directions and dimensions in neural activity space along which two regions may co-vary, suggesting that selective information relevant to the function of this specific interregional interaction can be transmitted via this communication subspace. Hence, only the population patterns that align and advance through this subspace would be maximally transmitted between areas.

Olfaction in mammals relies on communication between the olfactory bulb (OB) and the olfactory cortex (PCx; piriform cortex).[19–25] These areas are densely connected through long-range connections by which different odor features get transmitted. To date, subspace communication has not been analyzed in depth for pairs of odor-processing brain areas. Moreover, the properties of communication subspaces have been studied primarily in the neocortex, raising the question of how similar they might be in other cytoarchitectural designs (e.g., paleocortex like the OB and PCx). Therefore, the study of communication between the OB and PCx is likely to offer new insights into the general mechanisms of corticocortical interactions in the brain.

Among the factors influencing communication, temporal coordination of spiking activity plays a major role for interregional interactions. Sniffing patterns impose a natural rhythm to OB and PCx neurons,[22,26–32] coordinating local spiking activity and timing computations from a 300–500 ms window during rest to 100 ms during faster breathing rates.[33] Besides influencing local activity, it is widely recognized that the respiratory rhythm itself influences cognition, improving task performance[34,35] and regulating cognitive states.[36,37] Consistently, respiration-entrained brain oscillations are prominent in olfactory and associative areas (e.g., hippocampus,[38] prefrontal cortex[39]; somatosensory cortex[40]; amygdala[41]), suggesting that this rhythm may play a role in neuronal communication. Yet, we still do not fully comprehend how this rhythm influences communication at the neuronal firing scale.

Here, we address how population patterns are transmitted in the main olfactory pathway. Our results show that OB and PCx neurons interact through a communication subspace, which supports feedforward and feedback interactions and is entrained by the respiratory cycle,

[1]Departamento de Fisiología, Facultad de Medicina, Universidad de la República, Montevideo 11200, Uruguay
[2]Brain Institute, Federal University of Rio Grande do Norte, Natal, RN 59078, Brazil
[3]Monell Chemical Senses Center, Philadelphia, PA 19104, USA
[4]Lead contact
*Correspondence: joaqgonzar@gmail.com (J.G.), tort@neuro.ufrn.br (A.B.L.T.)
https://doi.org/10.1016/j.isci.2024.111275

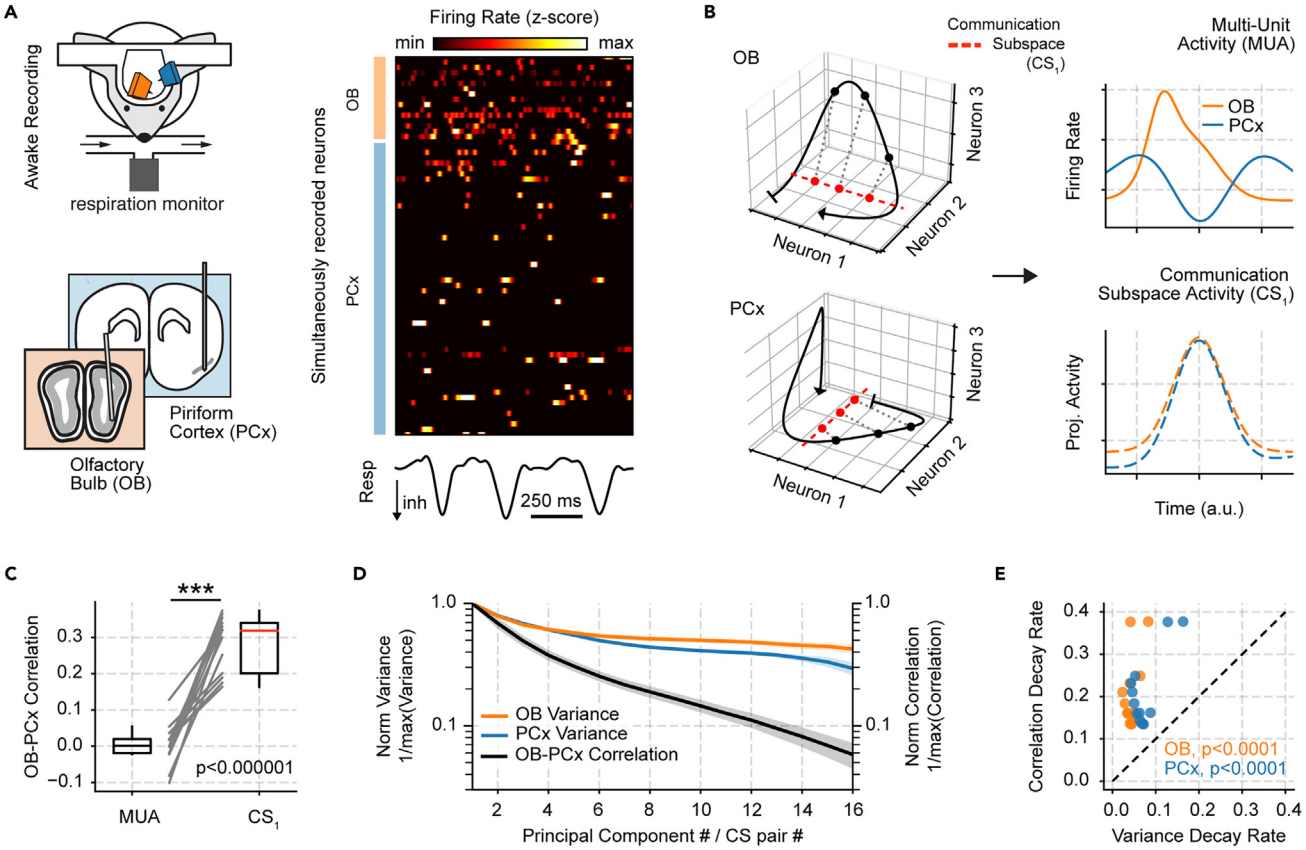

Figure 1. Characterizing the communication subspace between the olfactory bulb and piriform cortex

(A) Experimental recording scheme and probe localization in both olfactory areas (left panels; modified from[22]), and example single unit recordings along with the respiration signal (right).

(B) Toy model showing how canonical correlation analysis maximizes cross-area correlations. Canonical correlation achieves this by projecting the local state-space activity (black traces in left panels) to the subspace which maximizes cross-area correlations (CS_1 red dashed axis). Thus, this method allows to obtain maximally correlated signals across areas (bottom right panel), contrasting with MUA which lacks any correlation (top right panel).

(C) OB-PCx Pearson correlation for MUA and CS_1 signals. Boxplots show the median, 1st, 3rd quartiles, the minimum, and the maximum (excluding outliers); each line shows an individual session. $n = 13$ recording sessions from 12 mice. $^{***}p < 0.000001$, paired two-sided t-test.

(D) Normalized variance/correlation for each principal component number and CS pair (mean ± SEM; $n = 13$ recording sessions from 12 mice). For each recording session, variances and correlations were normalized by dividing each value by the maximum variance/correlation.

(E) Comparison of the variance and correlation decay for each recording session. The decays were calculated for the normalized variance/correlation as a function of the principal component number/CS pair using a negative exponential fit.

thus revealing how respiration influences spiking transmission. Moreover, experimental manipulations show that subspace activity can be triggered optogenetically and depends on the recurrent PCx connectivity to amplify and filter both OB and PCx responses. From a functional perspective, our results show that this communication channel is abolished during anesthesia and exploited in a flexible way during olfaction to transmit a low-dimensional representation of odor identity.

RESULTS

OB and PCx neuronal populations interact through a communication subspace

To understand communication in the main olfactory pathway, we first analyzed simultaneous recordings from OB and PCx populations performed during spontaneous (no odors presented) awake periods in head-restrained mice (Figure 1A). Because, in principle, any pairwise combination of neurons in each area might form a synapse, we employed canonical correlation analysis (CCA) to study the communication between these populations. Specifically, CCA seeks to maximize the correlation between 2 neuronal populations by finding a communication subspace (CS) in which to project local patterns to yield 2 CS activity signals that are maximally correlated (Figure 1B; see also Figure S1). In simpler words, the CCA approach identifies which subsets of neurons are correlated between the areas, and the communication subspace of each area is obtained by ascribing large (positive or negative) weights (hereafter referred as CS weights) to these neurons and low weights to uncorrelated neurons; finally, for each region, the CS activity is a signal obtained by the weighted sum of its neuronal activity as dictated by the

identified weights. Therefore, while the non-weighted summed activity (i.e., multi-unit activity, MUA) of each area may seem unrelated, a subset of correlated neurons (or several subsets) can be identified by the CS framework.

First, we validated the CS framework by studying a toy neuronal model in which we could control communication and local activity. We found that the CS could correctly identify individual subsets of communicating neurons between areas on a background of random local activity (Figures S1A and S1B). Moreover, different CS pairs captured the presence of independent linear combinations of neurons (i.e., independent subsets of correlated neurons) by ascribing different sets of weights for each combination (Figures S1C and S1D). These toy-model results provide a ground-truth reference for the use of CS.

When applying this framework to the OB-PCx data, we first identified how many significant CS pairs exist (Figure S2). To this end, we compared the correlation coefficient (R) of each CS pair against a surrogate distribution of R values computed by circularly time shifting the spiking activity of one of the populations by random amounts (Figures S2A and S2B). For each surrogate, we computed the CS and obtained the R for the first (i.e., most correlated) pair. We repeated this procedure 100 times for each session. We found that the first CS pair (CS_1) exhibited the largest correlation and that subsequent pairs showed an exponentially decaying distribution of correlation values (Figure S2C). When comparing against surrogates, only the first four CS pairs showed values above chance for all 13 recording sessions (Figure S2D). Nevertheless, for the remainder of the paper we focused on the first CS pair since it accounted for the largest correlation.

Notably, our results show that a communication subspace, and not global activity, explains neuronal correlations in the OB-PCx pathway. To contrast CS results, we compared the OB-PCx CS_1 correlation to the null hypothesis that the communication subspace is equivalent to the population activity (i.e., all neurons considered) in each area. To that end, we computed the MUA signal by summing all single neuron spikes in each area (employing the same time bins as used to compute the CS). Importantly, across all animals and sessions, OB-PCx CS_1 activity exhibited significantly higher correlations than the OB-PCx MUA (Figure 1C; $t(12) = 3.80$, $p < 0.000001$).

Furthermore, we show that the CS comprises only a "small region" of the state space of each area. To study how local activity compares to the OB-PCx CS, we matched the number of neurons in each area and computed Principal Component Analysis (PCA) and CS. We reasoned that by comparing the decay rates of the variances across principal components to the decay rate of the CS correlations, we can have an idea of how "big" or "small" the communication subspace actually is compared to the local population patterns. To allow comparisons, we normalized the variance of each principal component (by dividing it by the maximum variance across components) and the correlation from each CS pair (by dividing each value by the maximum correlation across pairs). Following this approach, we found that OB-PCx CS correlations decreased much faster than the individual variances of the principal components of each area (Figure 1D). We quantified the decay rate by a negative exponential fit of the normalized variances and correlations as a function of the component/CS pair number, which confirmed that OB-PCx correlations decrease significantly faster than the local variances (Fig, 1E, OB: $t(12) = 3.80$, $p < 0.000001$; PCx: $t(12) = 3.80$, $p < 0.0001$).

Respiration parses feedforward and feedback neuronal interactions

Next, we show that time-lagged interactions characterize CS communication. Since we reasoned that a genuine communication subspace should exhibit a non-zero time lag due to conduction and synaptic transmission delays (Figure 2A), we computed the CS using firing counts time-lagged between the regions (see also Figure S3 for a toy model validation), similar to the traditional cross-correlation analysis. Notably, under this analysis, we found that OB leads PCx activity by ~25 ms, the time lag with the highest correlation between both areas for CS_1 (Figure 2B). Thus, hereafter, we obtained all CS_1 signals by projecting the neuronal activity using the communication subspace calculated using this time delay; this only influences the neuronal weights of each CS_1 since neither the OB nor the PCx activity is lagged prior to the CCA projection. We further note that CS weights can be computed during a given time window and then applied to project population activity in a different period.

To determine whether the communication subspace exhibits directional interactions in the OB-PCx pathway that are not apparent from the global activity, we next computed the OB-PCx CS_1 cross-correlation (Figure 2C; red trace) and directionality (Transfer Entropy, TE; Figure 2D) and compared them to the same metrics applied to MUA (black trace). Specifically, TE calculates the reduction in uncertainty in the future values of a time series (e.g., OB activity) given the past values of another time series (e.g., PCx activity). The TE difference between both directions (OB→PCx vs. PCx→OB) is taken as the net directional information flow (see STAR Methods for details). We found that while OB leads PCx activity in the CS_1 projections, exhibiting a significant OB→PCx directionality (Figures 2C and 2D; $t(12) = 3.66$, $p = 0.003$ for ΔTE, paired two-sided t-test), the MUA results are more challenging to interpret due to the appearance of several peaks in the cross-correlogram (Figure 2C) and a non-significant directionality (Figure 2D; $t(12) = 1.66$, $p = 0.12$, paired two-sided t-test). Of note, the CS_1 directionality results also hold when computing CS_1 weights using non-lagged time series (Figure S4A).

Intrigued by the observation that all CS pairs, on average, exhibited a predominant OB→PCx direction and motivated by the well-described anatomical feedback from PCx→OB, we next investigated whether any evidence of feedback could be observed through CS_1 activity. To explore this, we divided the respiratory cycle into different phase bins and measured OB-PCx CS directionality in each phase bin. Notably, we observed a reversal in directionality during the course of the respiratory cycle (Figure 2E). Initially, following the start of inhalation, feedforward interactions predominated ($t(12) = 2.86$, $p = 0.01$). However, near the start of exhalation, PCx→OB feedback increased and became predominant during a short period ($t(12) = -2.65$, $p = 0.02$, paired two-sided t-test). Thus, despite the predominance of feedforward directionality, CS_1 also supports feedback interactions.

Respiration paces communication subspace activity

We next further characterized respiratory influences and found that, during spontaneous awake periods, the sniffing cycle entrains CS activity. First, we plotted raw and filtered CS_1 signals along with the nasal respiration recordings and observed each CS_1 signal to be rhythmically

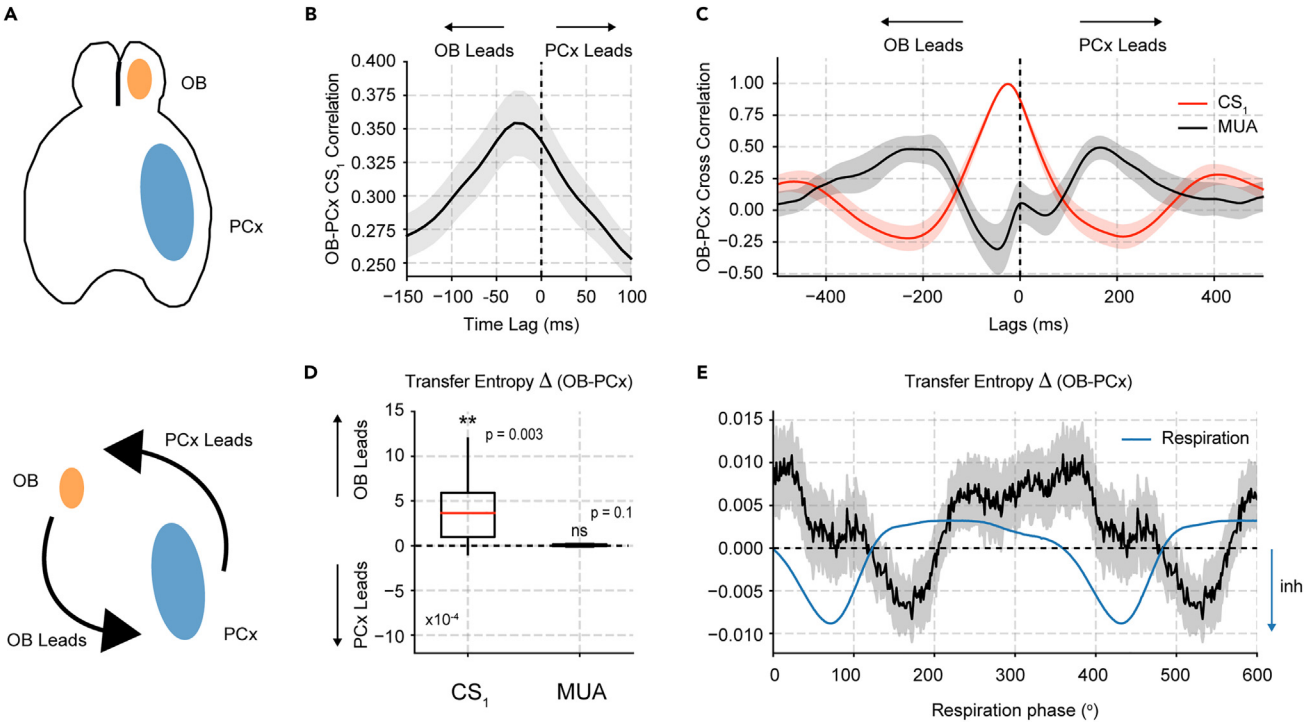

Figure 2. Measuring directionality in the OB-PCx communication subspace

(A) Schematic drawing depicting the OB-PCx pathway and their possible temporal relationships.

(B) CS_1 correlation as a function of the time delay between both areas (mean ± SEM; $n = 13$ recording sessions from 12 mice). Notice that by time-lagging one area against the other we find the temporal delay which maximizes the correlation.

(C) Cross-correlogram between both areas for the communication subspace (CS_1, red) and multiunit (MUA, black) activity (mean ± SEM; $n = 13$ recording sessions from 12 mice). The cross-correlation for each session was normalized by dividing it by its maximum value.

(D) Directionality analysis (Transfer Entropy) between both areas for CS_1 and MUA. The difference (delta) between OB→PCx and OB←PCx transfer entropy estimates is plotted for each signal. Boxplots show the median, 1st, 3rd quartiles, the minimum, and the maximum, $n = 13$ recording sessions from 12 mice; $^{**}p < 0.01$, paired two-sided t-test.

(E) Directionality analysis (Transfer Entropy) as function of the phase of the respiration signal (mean ± SEM; $n = 13$ recording sessions from 12 mice). As in panel D, the difference (delta) between both directions is plotted. Note a short period of directionality reversal from OB→PCx to OB←PCx at the start of expiration.

modulated by respiration (Figure 3A). These results hold across animals (Figure 3B). Note that the OB to PCx CS_1 lead was already evident in the raw (solid line), filtered (dashed line; 1–4 Hz), and averaged CS_1 signals (Figure 3B top left panel) within each breathing cycle. Consistently, both OB and PCx CS_1 signals show a prominent 2.5 Hz power spectrum peak (Figure 3B top right), coinciding with the respiratory peak frequency and coherent to the respiration signal (Figure 3B bottom). Of note, respiratory entrainment was not restricted to CS_1 and was also seen for subsequent CS pairs (Figure S4B). Interestingly, when contrasting CS_1 and MUA coherence to respiration, we found that both OB and PCx CS_1 are significantly more coupled to the respiratory activity (Figure 3B bottom; CS_1 vs. MUA OB-Resp Coherence: $t(12) = 6.02$, $p < 0.0001$; PCx-Resp Coherence: $t(12) = 5.12$, $p = 0.0002$, paired two-sided t-test), suggesting that respiration preferentially entrains subspace activity.

We next show that respiration drives CS_1 activity. We started by computing cross-correlograms between OB/PCx CS_1 signals and respiration. Importantly, we found that the cross-correlation function was not symmetrical and was heavily skewed toward negative lags, corresponding to respiration leading CS_1 activity in both areas. Note that, consistent with the previous OB-PCx directionality results, the OB CS_1 exhibited a shorter lag in the respiration cross-correlogram compared to the PCx CS_1.These results were confirmed through transfer entropy analysis showing significant Resp→CS_1 results for both OB and PCx (Figure 3C, right; OB: $t(12) = 6.19.$, $p < 0.0001$; PCx: $t(12) = 10.39$, $p < 0.000001$).

Besides finding respiratory entrainment of local CS signals, we further investigated whether OB-PCx correlations depend on the phase of the breathing cycle. This idea implies that maximal communication occurs during a specific phase of the respiratory cycle. To test this hypothesis, we binned the spontaneous CS_1 activity according to the respiratory phase and measured the OB-PCx CS_1 correlation in each phase bin (using different respiratory cycles as samples; Figure 3D). We found a significant modulation of the CS_1 correlations ($Z(12) = 4.26$, $p = 0.01$, Rayleigh test); in particular, correlations increased following the start of inspiration and then declined in the later part of the respiratory cycle (Figure 3E). Consistent with this result, OB-PCx CS_1 coherence showed a synchronization peak at the respiratory frequency (Figure 3E). Moreover, OB-PCx CS_1 coherence was significantly higher than OB-PCx MUA coherence (Figure 3E inset; OB-PCx Coherence: $t(12) = 7.97$,

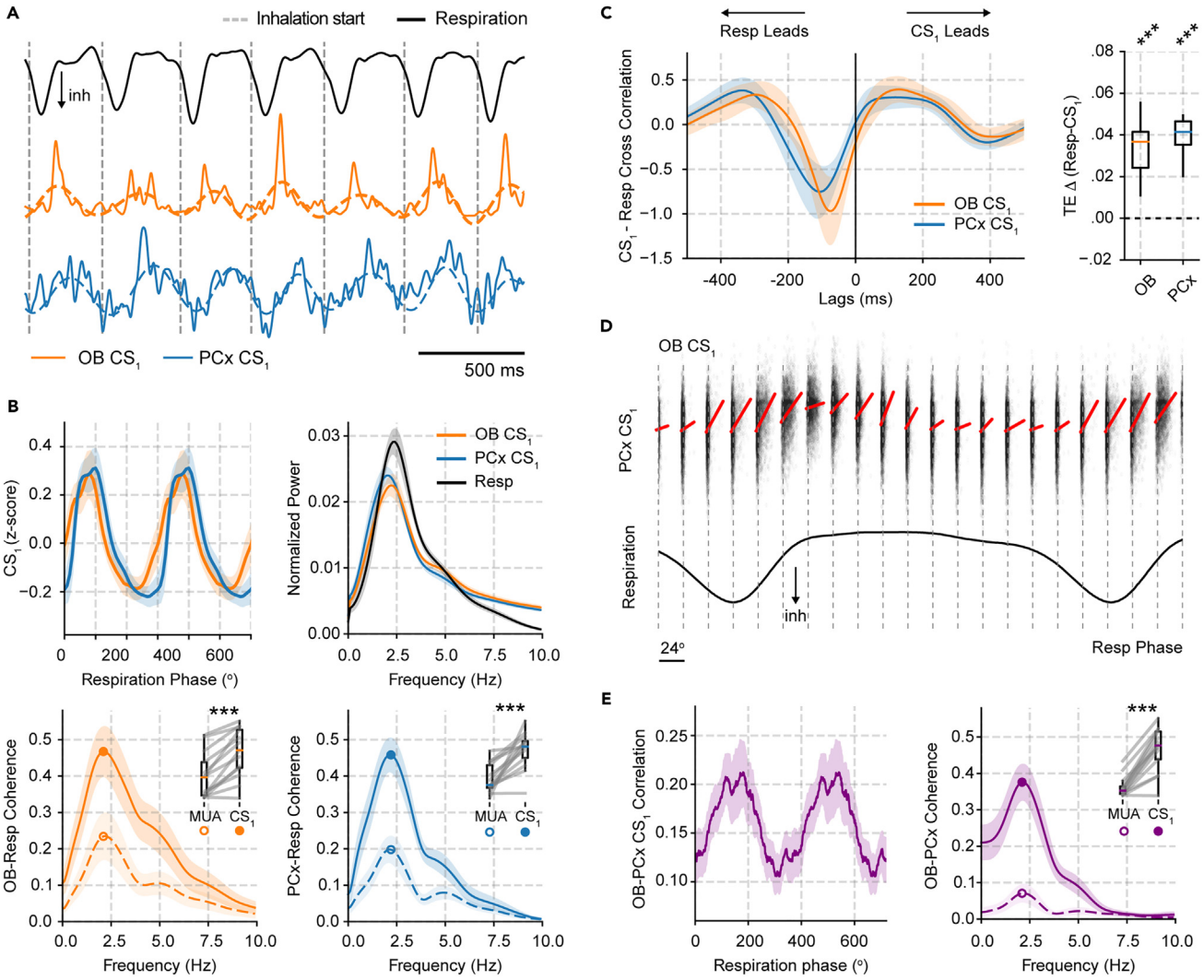

Figure 3. Respiration drives the activity of the communication subspace

(A) Left: Example of OB and PCx CS_1 along with the respiration signal. Dashed vertical lines indicate inhalation starts. Dashed colored lines show the 1–4 Hz filtered CS_1 for each area.

(B) Top Left: CS_1 as a function of respiratory phase (mean ± SEM; $n = 13$ recording sessions from 12 mice). Top Right: Power spectrum of the CS_1 and respiration signals (mean ± SEM; $n = 13$ recording sessions from 12 mice). Bottom: CS_1 and MUA coherence to respiration (mean ± SEM; $n = 13$ recording sessions from 12 mice). Insets: Boxplots comparing peak CS_1 and MUA coherence to respiration (frequency indicated by the dot); each line shows an individual session. Boxplots show the median, 1st, 3rd quartiles, the minimum, and the maximum (excluding outliers). ***$p < 0.001$, paired two-sided t-test.

(C) Left: Average cross-correlogram between respiration and OB/PCx CS_1 (±SEM; $n = 13$ recording sessions from 12 mice). Right: Directionality analysis (Transfer Entropy) between respiration and OB/PCx CS_1. The difference (Δ) between Resp→CS_1 and CS_1→Resp transfer entropy estimates is plotted for each signal. ***$p < 0.001$, paired two-sided t-test.

(D) OB-PCx CS_1 correlation as a function of the respiratory phase. The top panel shows an example correlation from a single recording session; the red lines show best linear fit for each respiratory phase. Below we show for the same recording session the average respiratory waveform.

(E) Left: CS_1 correlation (mean ± SEM; $n = 13$ recording sessions from 12 mice) during the respiratory cycle. Right: CS_1 and MUA OB-PCx coherence (mean ± SEM). Inset: Boxplots comparing CS_1 and MUA in the frequency indicated by the dot. ***$p < 0.001$, paired two-sided t-test.

$p < 0.0001$), further confirming that OB and PCx are likely to interact through a communication subspace and not through the global population.

CS membership relates to spiking phase preference during the respiratory cycle

Next, we show that CS_1 weights relate to the spiking phase preference of single neurons during the respiratory cycle. We plotted the average activity of all recorded cells in each area as a function of the respiratory phase and sorted them according to their CS_1 weights (Figure 4A).

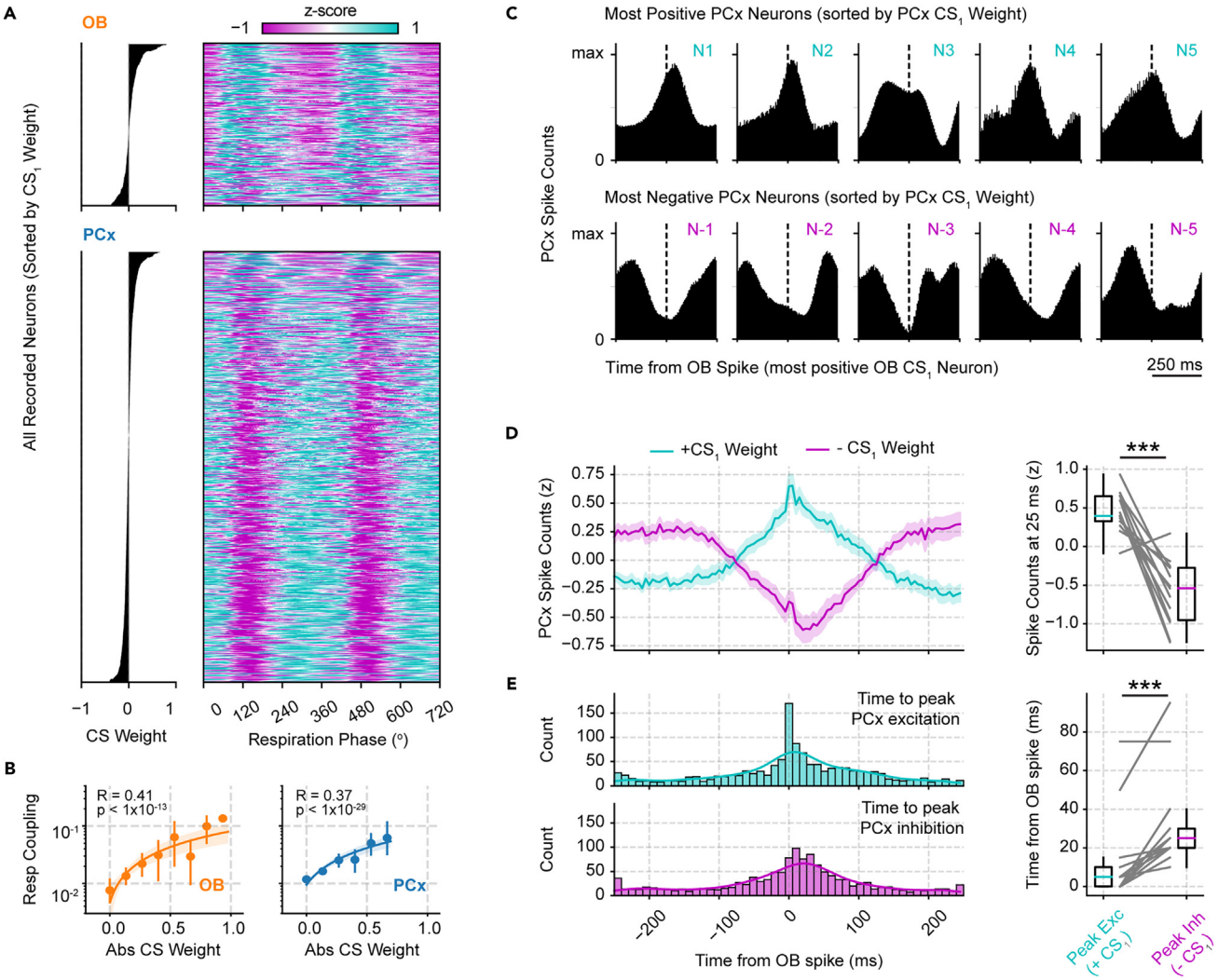

Figure 4. Excitatory-inhibitory spike relations characterize OB-PCx CS_1 communication

(A) Neuron spiking during each phase bin of the respiration cycle (right; 0° corresponds to the start of the inhalation); neurons are sorted according to the CS_1 weights (shown on the left panel). OB: 320 cells; PCx: 849 cells. We note that the respiratory phase tiling can also be observed by sorting cells according to their preferred phase (see Figure S5 and ref.[22] and [42]).

(B) Correlation between absolute CS_1 weights and the respiratory coupling strength (Modulation Index) of single cells. Note that bins were only employed for representational purposes. Error bars show the mean and 95% CI of the mean (n = OB: 320 cells; PCx: 849 cells).

(C) Example spike-spike cross-correlations between a single OB neuron (largest CS_1 weight) and 10 PCx neurons (top 5 most positive [top row] and negative [bottom row] CS_1 weights).

(D) Spike-spike cross-correlogram (mean ± SEM; $n = 13$ recording sessions from 12 mice) for the most positive OB vs. most positive (teal) and most negative (magenta) PCx CS_1 weighted neurons. Boxplot: Activity at the +25 ms time delay; Boxplots show the median, 1st, 3rd quartiles, the minimum, and the maximum (excluding outliers); each line shows an individual session. ***$p < 0.001$, paired two-sided t-test.

(E) Histogram showing the distribution of maximum excitation (teal) and maximum inhibition (magenta) times for the 10 most positive and 10 most negatively CS_1 weighted neurons across animals. Boxplot: Average time to maximum excitation/inhibition of positive/negative CS_1 weighted PCx neurons across animals. Boxplots show the median, 1st, 3rd quartiles, the minimum, and the maximum (excluding outliers); each line shows an individual session. ***$p < 0.001$, paired two-sided t-test.

We found that most OB neurons exhibited a single preferred respiratory phase near the inhalation start (40–140°), and that the most positive PCx neurons (+CS_1 weights) showed a similar phase preference to OB neurons. Nevertheless, the remaining PCx neurons (−CS_1 cells) exhibited an anti-phase pattern (that is, preferred the opposite phase than OB neurons or PCx +CS_1 cells). Moreover, the z-scored firing during the 40-140° respiratory phase significantly correlated with the CS_1 weights in both areas (OB: R = 0.23, $p < 0.0001$; PCx: R = 0.34, $p < 1 \times 10^{-20}$). Note that while +CS_1 cells in either region exhibited similar firing levels during this phase bin, −CS_1 cells fired close to baseline in the OB and decreased their average spiking in the PCx (Figure 4A). Consistently, the distribution of CS_1 weights was skewed toward negative values in the

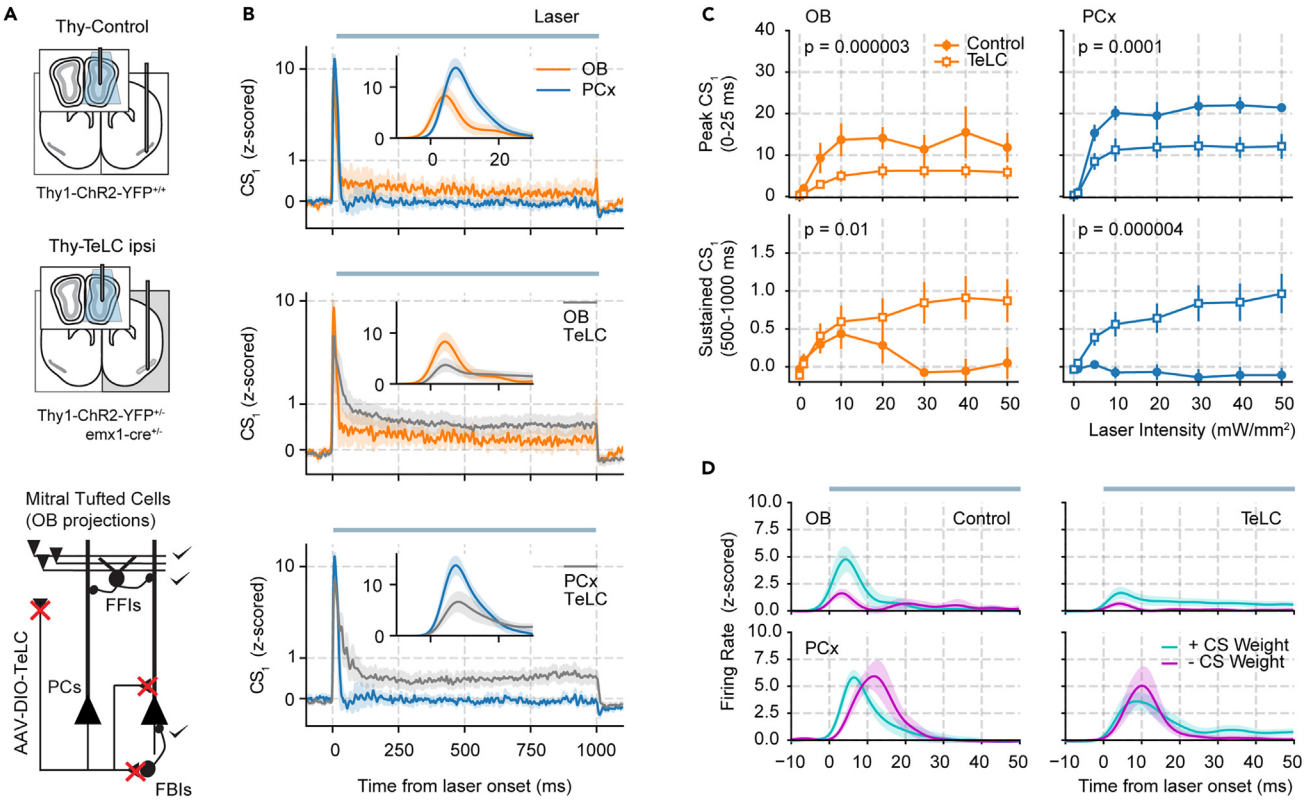

Figure 5. Probing the mechanisms behind the OB-PCx communication subspace

(A) Top: Experimental recording conditions for each group. OB and PCx recordings were made from the hemisphere containing TeLC expression (modified from[22]) during optogenetic stimulation of the OB (laser duration = 1 s). Bottom: Schematic of circuit changes after TeLC expression in principle cells (PCs) of the piriform circuit (MTCs: mitral/tufted cells; FFIs: feedforward interneurons; FBIs: feedback interneurons). TeLC expression blocks synapses from PCx principal cells (red crosses).

(B) OB and PCx CS_1 activity triggered by optogenetic stimulation of OB projecting neurons (mean ± SEM; Control: $n = 5$ recording sessions from 5 mice; TeLC: $n = 14$ recording sessions from 7 animals). Insets highlight the initial response.

(C) CS_1 activity as a function of the laser intensity (mean ± SEM Control: $n = 5$ recording sessions from 5 mice; TeLC: $n = 14$ recording sessions from 7 animals). The laser stimulation period was divided into an initial (0–25 ms) and a sustained response (500–1000 ms). p values were obtained from a two-way ANOVA test.

(D) Triggered spiking activity of "positive" and "negative" cells according to their CS_1 weights (mean ± SEM Control: $n = 5$ recording sessions from 5 mice; TeLC: $n = 14$ recording sessions from 7 animals). The most positive and most negative cell from each session was employed here. The panel shows a zoom-in view of the first 50 ms following laser onset.

PCx, corresponding to the large majority of (likely inhibited) anti-phase neurons, and was significantly different from the CS_1 weight distribution of OB ($D(110) = 0.12$, $p < 0.0001$, Kolmogorov-Smirnov test). Importantly, we found a significant correlation between the absolute CS_1 weights and the respiratory coupling strength of single cells (Figure 4B, OB: $R = 0.41$, $p < 1 \times 10^{-13}$; PCx: $R = 0.37$, $p < 1 \times 10^{-29}$), suggesting that respiration preferentially entrains communicating neurons in both areas.

We next show that putative excitatory and inhibitory interactions explain CS_1 weights. First, we selected the most positive CS_1 OB neuron from a representative recording and analyzed the spike counts of the top five $+CS_1$ and $-CS_1$ PCx cells. We found that the $+CS_1$ PCx cells tended to spike shortly after OB spikes, while $-CS_1$ PCx cells tended to be inhibited (Figure 4C). This result was consistent across animals when analyzing the top ten $+CS_1$ OB neurons against the top ten $+CS_1$ and $-CS_1$ PCx neurons (Figure 4D, $t(12) = 7.38$, $p < 0.001$). Note that inhibition occurred later compared to excitation in the PCx ($t(12) = 2.25$, $p < 0.001$; Figure 4E), suggesting that inhibition, on average, may take more synaptic steps than excitation. These results suggest that subspace interactions and respiratory firing phase preferences are likely to be intrinsically related.

OB-PCx communication subspace interactions depend on intact synaptic connectivity

We next demonstrate that, as expected based on the dense anatomical connectivity, direct communication underlies OB-PCx subspace interactions. To this end, we analyzed CS_1 activity during optogenetic stimulation of OB excitatory cells (Figure 5A). For these analyses, we calculated CS_1 weights employing the laser stimulation periods. We found that light stimulation caused a large amplitude, transient CS_1 response (Figure 5B). As expected, the transient response first occurred in the OB CS_1 activity and appeared after a short <10-ms latency

in the receiving PCx population (Figure 5B; Time to CS_1 peak: t(4) = 5.65, $p = 0.004$, paired two-sided t-test), confirming the predominant OB-PCx communication directionality. In the OB, the transient response was followed by a lower amplitude sustained activity lasting through the entire stimulation period (Figure 5B). Noteworthy, the spontaneous activity of the cells identified during laser stimulation also exhibited the phase-antiphase CS_1 spike pattern segregation within respiratory cycles (Figure S6) as found in our earlier analysis (cf. Figure 4A).

Next, we show that (1) recurrent excitation within the PCx amplifies the initial (transient) CS_1 response, (2) lateral inhibition shuts down the sustained component of the CS_1 response, and (3) feedback projections from the PCx influence OB CS_1 activity. To probe these mechanisms, we compared control animals with animals expressing TeLC in the PCx. TeLC expression blocks all synapses from PCx principal cells while preserving principal cell excitability (i.e., from afferent inputs),[22] allowing us to probe how local PCx interactions shape the CS_1 activity in response to optogenetic stimulation of the OB (Figure 5A). Notably, we found that the initial, transient CS_1 response (0–25 ms) decreased in both areas of TeLC-infected animals (Figures 5B and 5C). Interestingly, however, the sustained CS_1 response (500–1000 ms) increased significantly also for both areas in the TeLC group (Figure 5C; note that the sustained response is nonexistent in the PCx of control animals). Hence, these results causally demonstrate that OB-PCx subspace communication involves both feedforward (OB→PCx) and feedback (PCx→OB) projections, with the latter conclusion inferred from the fact that altering PCx connectivity alters OB CS_1 activity. These results are consistent with previous connectivity and imaging studies performed in this system.[19,20,43]

We next compared the activity of the most positive and negative CS weighted cells following OB stimulation (Figure 5D). In control animals, $+CS_1$ OB cells fired more than $-CS_1$ cells during the first 25 ms (t(4) = 4.08, $p = 0.01$, paired two-sided t-test). In addition, $+CS_1$ PCx cells fired earlier than $-CS_1$ cells (t(4) = 3.98, $p = 0.01$, paired two-sided t-test). In TeLC recordings, $+CS_1$ and $-CS_1$ OB cells showed a similar firing rate difference as in control animals (t(13) = 2.14, $p = 0.04$, paired two-sided t-test). On the other hand, the time difference previously observed for $+CS_1$ and $-CS_1$ PCx cells disappeared in TeLC animals (t(13) = 0.17, $p = 0.86$, paired two-sided t-test). Thus, these results suggest that $+CS_1$ PCx cells actively recruit inhibition and suppress $-CS_1$ spiking during the first 10 ms of OB laser stimulation, leading to their different spike time-courses, and that, consequently, this effect is lost in TeLC recordings due to the lack of feedback inhibition recruitment.

Anesthesia disrupts OB-PCx subspace communication

Next, we show that subspace communication depends on the cognitive state and, consequently, is altered during anesthesia. First, we compared CS_1 correlations between awake and ketamine/xylazine anesthesia recordings. For this analysis, we computed CS_1 weights during awake periods and used them to project neuronal activity during anesthesia (Figure 6A). We found that CS_1 correlations significantly decreased during loss of consciousness (Figure 6B left; t(9) = 4.44, $p = 0.001$, paired two-sided t-test), confirming that the subspace that allowed for communication during wakefulness no longer does during anesthesia. Thus, this result suggests a cognitive role for CS_1 communication.

Moreover, we analyzed how neuronal communication occurs during anesthesia and found that a new CS emerges unrelated to the awake channel. For these analyses, we computed CS weights exclusively using neuronal activity during anesthesia and compared them to the awake subspace weights. Interestingly, we found that both subspaces accounted for similar correlation gains above MUA correlations (Figure 6B right; t(9) = 0.13, $p = 0.89$, paired two-sided t-test). This control is important since MUA correlations greatly increased during anesthesia (Figure 6B middle; t(9) = 3.76, $p = 0.004$, paired two-sided t-test). Notably, anesthesia and awake CS_1 weights were not positively correlated (Figure 6C, OB: R = −0.17, $p = 0.02$; PCx: R = 0.01, $p = 0.8$, Pearson correlation), confirming that different groups of neurons communicate within each state. Moreover, despite respiratory entrainment of single neurons significantly increasing during anesthesia (Figure 6D, left panel, OB: t(247) = 10.46, $p = 1.9 \times 10^{-21}$; PCx: t(652) = 20.0, $p = 1.1 \times 10^{-69}$, paired two-sided t-test), the CS_1 weights were not positively correlated with the level of respiratory coupling in this state (Figure 6D, right panel, OB: R = −0.13, $p = 0.04$; PCx: R = −0.05, $p = 0.22$, Pearson correlation), contrasting therefore with the results obtained for the awake CS_1 (cf., Figure 4B). The lack of positive correlation between CS weights and spike-respiration coupling during anesthesia (despite the overall coupling increase) demonstrates that respiratory CS entrainment is not a mere consequence of high respiratory modulation of single cells, and further suggests a cognitive role for the differential respiratory entrainment of communicating cells.

Olfactory communication occurs through a general and a specialized channel

We investigated the functional role of the OB-PCx CS and show that communication during olfaction occurs through a general ("spontaneous" CS_1) and a specialized channel ("odor" CS_1). We took two complementary approaches in these analyses: we derived CS weights exclusively during either (1) spontaneous periods or (2) during odor sampling. We found that spontaneous CS_1 and odor CS_1 weights were weakly but significantly correlated (OB: R = 0.3, $p < 1 \times 10^{-7}$; PCx: R = 0.3, $p < 1 \times 10^{-18}$; Figures S7A and S7B). Prior to analyzing group data of CS_1 activity, we multiplied all CS_1 traces by the sign of their response to odors; this was necessary since two animals exhibited CS_1 activity decreases to odors in both areas (Fig.S8) and we wanted to study changes in the magnitude of CS_1 activity. When analyzing odor and odorless sniffs, we found an increase in both the spontaneous and odor CS_1 activity magnitude during odor sampling in both areas (time-stamps marked by blue and orange dots in Figure 7B; $p < 0.05$, paired one-sided t-test). Note that odor CS_1 showed a more sustained odor-evoked response (0–200 ms) compared to the spontaneous CS_1 (Figure 7B).

Notably, we observed a functional switch in CS communication during odor presentations. Namely, OB-PCx spontaneous CS_1 correlations decreased during odor presentations compared to odorless periods (Figures 7C and S7; t(12) = 5.29, $p = 0.00019$, paired two-sided t-test), while odor CS_1 correlations increased (Figure 7C, t(12) = 7.21, $p = 0.00001$, paired two-sided t-test). These changes were accompanied by a

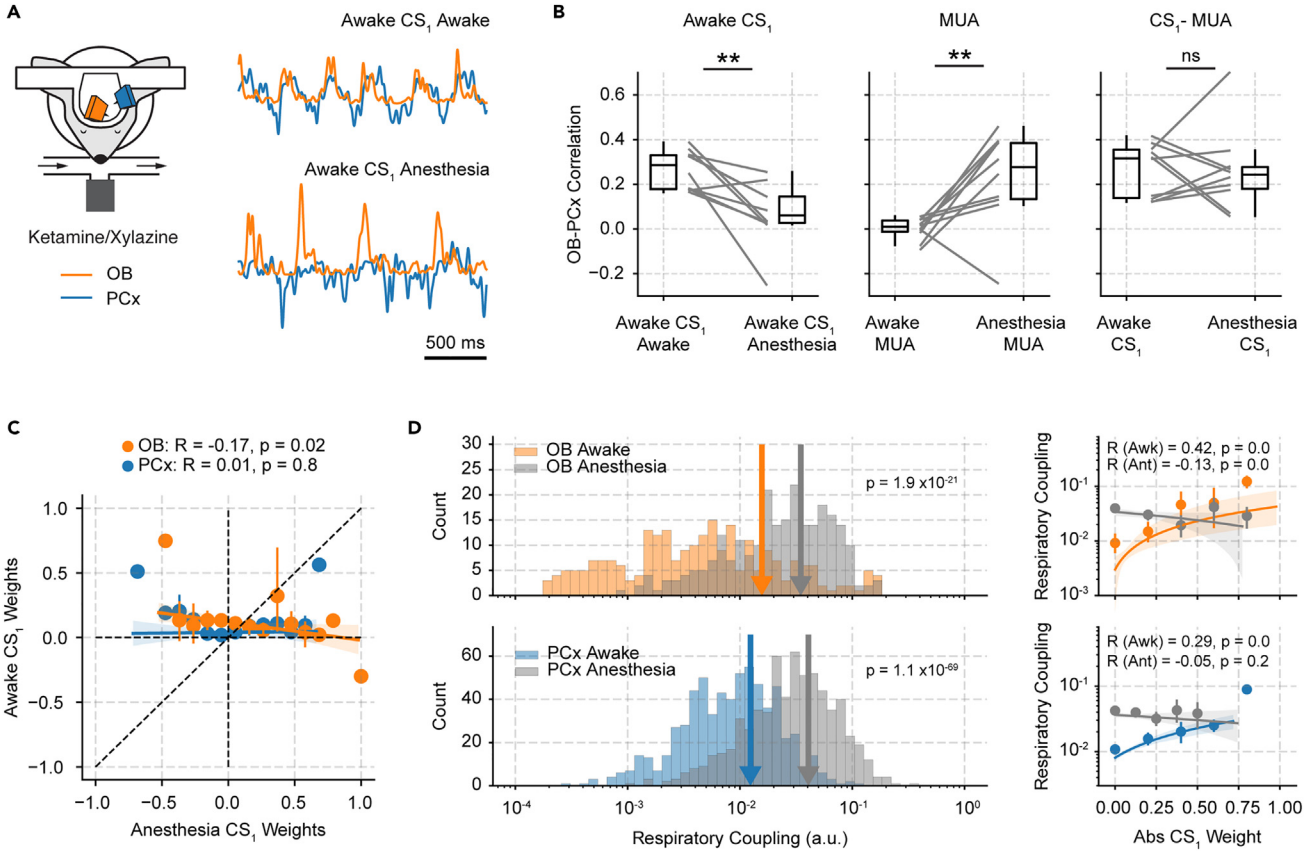

Figure 6. Ketamine-xylazine anesthesia alters CS_1 communication

(A) Example CS_1 traces during head-fixed wakefulness and after ketamine-xylazine anesthesia. CS_1 weights were computed during awake periods and later used to project neuronal activity during anesthesia.

(B) Left: OB-PCx CS_1 correlation during awake and anesthesia periods. CS_1 weights were computed during awake periods and later used during anesthesia, as in the previous panel. Right: OB-PCx CS_1 correlation, but with anesthesia CS_1 weights computed during anesthesia. Boxplots show the median, 1st, 3rd quartiles, the minimum, and the maximum (excluding outliers); each line shows an individual session. n = 10 recording sessions from 9 mice. Of note, since OB-PCx correlations largely increase during anesthesia, CS_1 correlations were normalized by subtracting the OB-PCx MUA correlation. $^{**}p < 0.01$, paired two-sided t-test.

(C) Correlation between CS_1 weights computed exclusively during awake and anesthesia periods. Error bars show the mean and 95% CI of the mean (OB: 248 cells; PCx: 653 cells).

(D) Left: Distribution of respiratory coupling strength (Modulation Index) for all single cells during awake and anesthesia recordings. The vertical arrows show the distribution mean for each case. p was obtained from a paired two-sided t-test. Right: Correlation between absolute CS_1 weights and the respiratory coupling of single cells. Note in C and D that bins were only employed for representational purposes. Error bars show the mean and 95% CI of the mean (OB: 248 cells; PCx: 653 cells).

significant decrease in OB→PCx directionality during odor sampling for the spontaneous CS_1 (Figure 7C; $t(12) = 3.29$, $p = 0.006$, paired two-sided t-test) and a significant increase in OB→PCx directionality for the odor CS_1 (Figure 7C; $t(12) = 3.84$, $p = 0.002$, paired two-sided t-test).

We next analyzed spontaneous CS_1 activity in response to increasing concentrations of a single odorant (Figure S9A). Our results showed that for both spontaneous and odor CS_1, OB activity increased with odorant concentration, while PCx did not (Figure S9A). Nonetheless, spontaneous OB-PCx CS_1 correlations decreased as concentration increased, while odor CS_1 correlations did not depend on concentration (Figure S9B). Thus, these results further suggest that communication during olfaction involves a mixture of a common (concentration-dependent) and a specialized (concentration-independent) channel.

Odor identity is transmitted through the communication subspace

Finally, we demonstrate that the OB-PCx CS transmits odor identity as a low-dimensional representation. We analyzed the activity of several CS pairs since odors are likely represented by different neuronal combinations spanning multiple CS pairs (recall that independent linear combinations give rise to different CS pairs; Figures S1C and S1D). When plotting the average amplitude of three CS pairs for the presentation of 2 different odorants (0–500 ms after inhalation, 0.03, 0.01, 0.3, 1.0 v./v. concentrations), we found that regardless of concentration, different

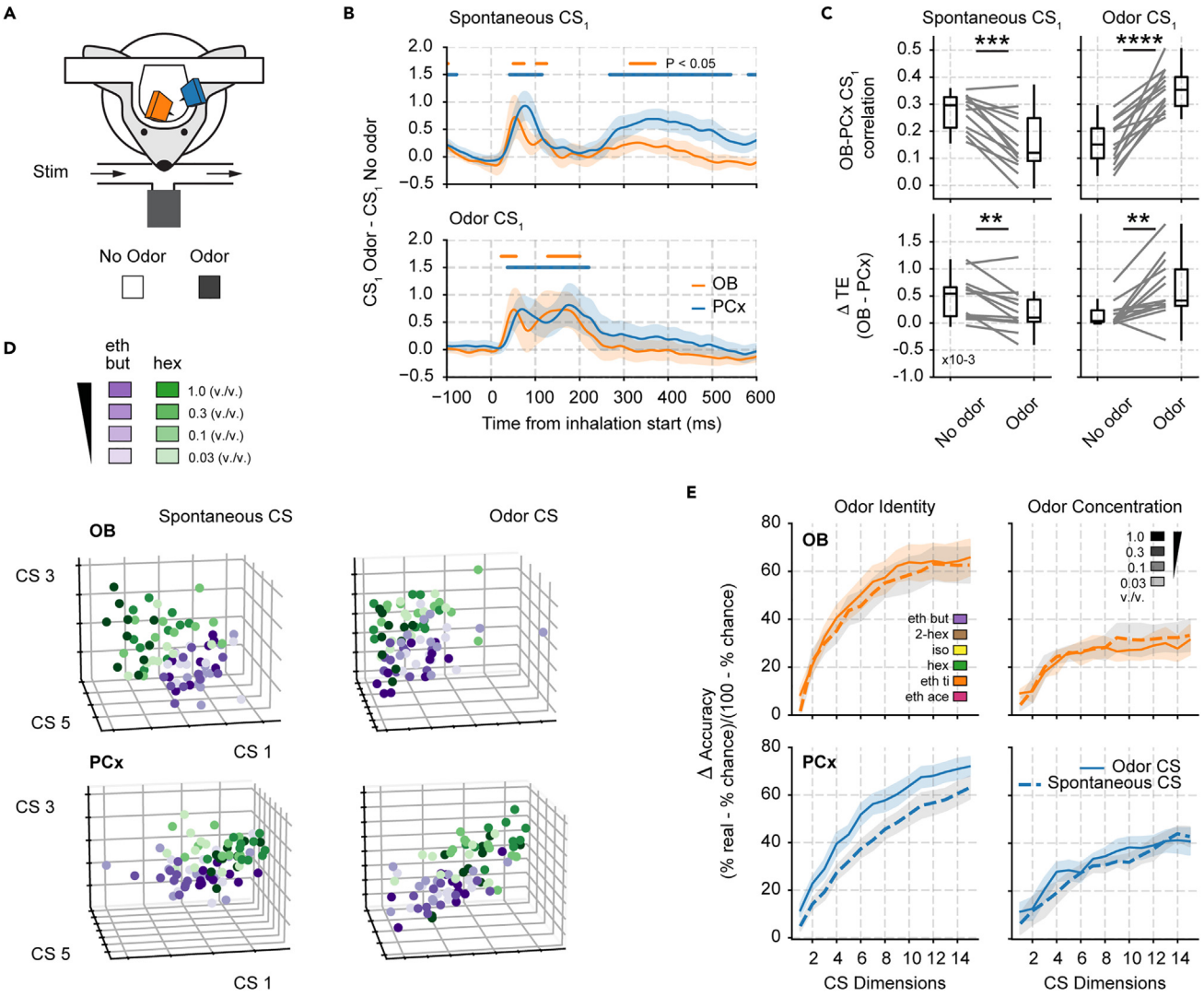

Figure 7. The OB-PCx communication subspace allows the transmission of odor identity

(A) Experimental recording scheme and odor panel employed in the experiments (modified from[22]).

(B) CS_1 activity difference (between odor and odorless sniffs) triggered by inhalation start (mean ± SEM; n = 13 recording sessions from 12 mice). Dots indicate significant differences, $p < 0.05$, paired one-sided t-test.

(C) Top: OB-PCx CS_1 correlations after odor and no odor sniffs. Bottom: Directionality analysis (Transfer Entropy) between both areas for CS_1 during odor and odorless sniffs. The difference (delta) between OB→PCx and PCx→OB transfer entropy estimates is plotted for each condition. Boxplots show the median, 1st, 3rd quartiles, the minimum, and the maximum (excluding outliers). Each line shows an individual session (n = 13 recording sessions from 12 mice). **$p < 0.001$, paired two-sided t-test.

(D) Example CS activity for 3 CS pairs from a representative animal obtained during the presentation of 2 different odorants at different concentrations. Each dot shows the average CS activity (0–500 ms following inhalation start) during an individual trial. Note the clustering of purple shaded vs. green shaded points, indicating odor separation.

(E) Identity/concentration decoding accuracy (mean ± SEM; n = 13 recording sessions from 12 mice) as a function of the number of aggregated CS pairs ("CS dimensions") considered for the analysis. The data employed consisted of the average CS activity (for each dimension) during the first 500 ms following inhalation start. For all panels, CS_1 weights were computed either during exclusive no odor sniffs (spontaneous CS_1) or exclusively during odor sniffs (odor CS_1).

odors segregated in this low-dimensional subspace (Figures 7D and S10). Similar results held for 6 odorants at equal concentrations (Figure S11). Importantly, the intersection of odor clusters likely suggests that the transmission of odorant identity occurs through overlapping, not independent, combinations of neurons (Data. S1).

Subsequently, we trained and tested a linear decoder employing all available odor presentations to either decode identity from a six-odorant panel at 0.3 v./v. concentration or decode concentration from a two-odorant panel at 0.03, 0.1, 0.3, 1.0 v./v. As shown in Figure 7E, we successfully decoded identity and concentration above chance levels (1/6 for odors, 1/4 for concentrations) for increasing combinations of

CS pairs (i.e., CS_1, [CS_1,CS_2], [CS_1,CS_2,CS_3], etc.; $p < 0.05$ for all dimensions >2, one sample t-test against chance levels). Comparing identity and concentration decoding (note the normalization of accuracies to their chance levels), we found that CS activity was significantly more specific to odor identity than concentration (OB Odor CS: $F(1,14) = 93.2$, $p < 10^{-18}$; OB Spontaneous CS: $F(1,14) = 64.13$, $p < 10^{-13}$; PCx Odor CS: $F(1,14) = 133.1$, $p < 10^{-24}$; PCx Spontaneous CS: $F(1,14) = 49.1$, $p < 10^{-10}$, two-way ANOVA). Importantly, when comparing spontaneous and odor CS identity decoding accuracies, we found for the PCx that its odor CS provided significantly better decoding results than the spontaneous CS ($p < 0.05$ for all dimensions, paired two-sided t-test), confirming that the olfactory cortex likely employs both a general and a specialized channel for representing odor.

DISCUSSION

Here, we addressed how population patterns are transmitted in the main olfactory pathway. Our results unveil that a low-dimensional shared subspace (i.e., a communication subspace) forms the major communication channel between OB and PCx neuronal populations. Notably, this communication subspace is paced by nasal respiration and allows feedforward and feedback interactions to occur in different phases of the sniffing cycle. We show that subspace activity can be commanded by OB optogenetic stimulation and that it depends on lateral excitation and inhibition in the PCx to shape initial and sustained responses.

From a functional perspective, our results suggest a cognitive role for CS communication since (1) anesthesia disrupts CS communication, (2) subspace activity increases during odor sampling, and (3) this communication channel transmits a low-dimensional representation of odor identity. This low-dimensional representation carries more identity than intensity information, consistent with previous experimental results,[22] though concentration information could still be decoded above chance from CS activity, also consistent with experimental and modeling results.[23,44]

Notably, several of our results can be related to the primacy theory of odor perception.[45] Under this model, early (concentration stable) activated OB cells encode odor identity and transmit identity information to the PCx. OB cells activated later (more sensitive to concentration) would be suppressed through feedback inhibition in the PCx. These ideas are consistent with the abovementioned results and with CS_1 OB latencies decreasing with increasing concentration (Figure S9), as also observed in previous OB recordings.[45] Thus, these results suggest that the primacy coding cells may take part in subspace communication.

Moreover, the primacy model might also explain why concentration information may not be accurately represented by CS members. Under this scenario, later responding cells carry more concentration information, but their influence would be suppressed by feedback inhibition within the PCx and through centrifugal projections targeting interneurons in the OB (Figures 5B and 5C and ref. 19,21,22). As a result, concentration information would not be a main feature encoded by the conjoint activity of OB-PCx subspace members, though it is present in their activation latency (Figure S9). On the other hand, concentration information transmission might be more prevalent in other OB subspaces, for instance, in those presumably established with the anterior olfactory nucleus.[19]

CS analysis offers a comprehensive view of neuronal interactions in the OB-PCx pathway

Several factors complicate our understanding of the olfactory system and how its neurons communicate and represent smell across all major olfactory hubs. One significant challenge is its spatial heterogeneity. Olfactory sensory neurons (OSNs) located in the olfactory epithelium, each expressing a single olfactory receptor, converge into functional units known as glomeruli inside the OB.[46] Despite the order in OSN projections, OB glomeruli lack a detailed chemotopic structure and only exhibit some coarse organization.[47] Mitral and tufted cells (MTCs) contact these glomeruli and project to other olfactory centers, sending spatially diverse projections, principally to the PCx.[19,20,22,25,43,48–51] Consequently, the PCx inherits this lack of a chemotopic map, meaning that the same odorant can activate neurons in distant sites of the same area.[20,28,48,49,52–54]

To identify coordinated neuronal assemblies across these areas, we analyzed the OB-PCx CS, similar to recent efforts in the visual and motor systems.[11–14] This analysis allowed us to pinpoint groups of cells across areas that exhibit maximal correlation in time and form functional partnerships following each sniff. Crucially, by examining the CS weights of each neuron, we could differentiate between putative excitatory and inhibitory relationships occurring during the respiratory cycle. Although CS weights could be attributed to respiratory phase preferences, the inactivation of the local piriform recurrent circuitry demonstrated that local inhibition causes the firing pattern differences between +CS and −CS cells. Therefore, our results suggest that subspace interactions and the respiratory firing phase preference of single cells are likely to be intrinsically related.

Respiration drives neuronal communication

It has become increasingly clear that the respiratory rhythm influences the activity of a wide variety of brain areas – well beyond olfactory centers.[27,33,34,38,40,41,55–59] This rhythm, impacting faster local oscillations,[26,27] is proposed to play a role in integrating information across the brain.[33,60] Our findings provide direct support for this notion by demonstrating at the neuronal level that: (1) respiration exerts a more pronounced modulation on local communication subspace (CS) activity compared to multi-unit activity (MUA), (2) absolute CS weights predict respiratory entrainment of individual cells only during awake recordings, and (3) respiration modulates synchronization between the OB and PCx within the communicating populations. These results highlight the direct impact of this body rhythm on neuronal communication in the main olfactory pathway, suggesting it may also serve similar functions in other upstream areas.

How does respiration influence interregional communication? Our study suggests that it does so by modulating specific directions in neural state-space that define the CS. Additionally, and possibly related, by providing a window of enhanced temporal coordination (most likely in the source population, i.e., the OB), the respiratory rhythm would favor spike transmission. This would occur because synchronous inputs have a higher probability of firing a target neuron than asynchronous inputs.[9,61,62] Hence, we suggest that the combination of subspace communication and temporal coordination might be a canonical strategy to facilitate corticocortical interactions.

We note that our results were obtained in head-fixed mice; as such, future studies should address if subspaces are employed during more naturalistic conditions. For example, analyzing an odor-discrimination task could provide further insights into how this communication channel might be used for information routing. We hypothesize that subspace interactions within breathing cycles aid odor discrimination, allowing flexible switches between sensory-driven and action-oriented neuronal communication.

Directionality in the canonical olfactory pathway

Long-range loops play a crucial role in various sensory and motor systems across the brain.[63,64] In olfaction, the primary long-range pathway is formed by the connection from the OB to the PCx, although other significant loops exist (e.g., OB to anterior olfactory nucleus).[19,22,48,52] Traditionally, these pathways are conceptualized in terms of their information flow[8,12,65] as either feedforward (proceeding from the lower sensory area to a higher area, as in the case of OB → PCx) or feedback (going from the higher to the lower sensory area, as in the case of PCx → OB). Our results demonstrate that while feedforward interactions are predominant, feedback also occurs in the OB-PCx communication subspace, constituting a genuine loop. Notably, feedforward communication primarily occurred during inhalation, while feedback took place in a brief window during exhalation. This result contrasts with subspace properties described in the neocortex, where different CS pairs support different directions of communication,[12] suggesting that subspace characteristics may depend on the cytoarchitectural design.

Furthermore, by analyzing how the local recurrent PCx circuit affects CS activity, we were able to show that PCx activity inhibits OB neurons (Figure 5B, inferred from TeLC recordings showing a higher sustained OB response compared to control), consistent with previous reports showing that the excitatory centrifugal PCx output contacts granule cells within the OB and produces inhibition.[19,21] From a functional perspective, previous results showed that PCx inhibition into OB decorrelates odor representations in this area and changes the tuning properties of single cells.[21] This mechanism could potentially explain why OB-PCx spontaneous CS correlations decrease during odor stimulation. Under this scenario, during odor presentations PCx feedback changes OB activity, thereby promoting communication through the odor specific channel and decreasing communication through the spontaneous CS.

Spontaneous vs. evoked activity and the representation of odor in the main olfactory pathway

How does spontaneously organized neural patterns relate to stimulus-driven activity? Through an examination of spontaneous communication and subsequent analysis of how these patterns change with sensory stimuli, we demonstrate that neuronal populations exhibiting spontaneous correlation also transmit odor information during sensory stimulation. Additionally, we observed that certain neuronal groups seem to communicate more robustly during odor stimulation, evidencing the recruitment of additional neurons during olfaction, a result evidenced more strongly in the PCx, where the odor CS contained more odor identity information than the spontaneous CS.

A possible interpretation of these results is that spontaneously correlated neurons form a fundamental scaffold for olfaction, providing a "good-enough" odor representation. On the other hand, neurons that communicate exclusively during odor stimulation contribute finer-grained details, enriching the overall representation. In support of these ideas, data from flies and mice shows that odor encoding populations fall between two extremes, either exhibiting reliable firing patterns across trials or displaying high trial-to-trial variability.[66] The former property potentially adds robustness of the code while the latter might add discriminatory power.

Limitations of the study

This study has several limitations to consider when interpreting our results. First, animals were recorded under head-restricted conditions. Thus, future studies should address how subspace communication changes during freely moving conditions under varying respiratory frequencies. Second, the absence of a behavioral task limits understanding of how animals utilize subspace communication during behavior. Exploring this subject could be particularly important, as subspace communication is thought to be a flexible information routing mechanism. Finally, we did not have the means to identify how different neuronal subgroups in the OB and PCx contribute to subspace activity. Therefore, elucidating the distinct contributions of each cell type is likely to provide important insights into communication within this system and the brain as a whole.

RESOURCE AVAILABILITY

Lead contact

Additional information and requests for resources and reagents should be sent and will be fulfilled by the lead contact, J.G. (joaqgonzar@gmail.com).

Materials availability

This study did not generate new unique reagents.

Data and code availability

- Data: All the data employed came from the previously Published Datasets: Bolding and Franks, 2018b Collaborative Research in Computational Neuroscience. 'Simultaneous extracellular recordings from mice OB and PCx and respiration data in response to odor stimuli and optogenetic stimulation of OB'. Accession numbers are listed in the key resources table.
- Code: Codes have been deposited at GitHub and Zenodo and are publicly available as of the date of publication. Accession numbers are listed in the key resources table.
- Additional information: Any additional information required to reanalyze the data reported in this paper is available from the lead contact upon request.

ACKNOWLEDGMENTS

We thank Diego Laplagne and Vitor Lopes-dos-Santos for their critical reading of our manuscript. JG was supported by Comision Academica de Posgrado (CAP), Programa de Desarrollo de Ciencias Básicas (PEDECIBA), Comisión Sectorial de Investigación Científica (CSIC), and a Ben Barres Spotlight Award by eLife. P.T. was supported by PEDECIBA and CSIC. K.A.B. was supported by the Monell Chemical Senses Center and by National Institute on Deafness and Other Communication Disorders grant R01DC020927. A.B.L.T. was supported by Conselho Nacional de Desenvolvimento Científico e Tecnológico (CNPq), Coordenação de Aperfeiçoamento de Pessoal de Nível Superior (CAPES), and the Alexander von Humboldt Foundation.

AUTHOR CONTRIBUTIONS

J.G.: Conceptualization, Software, Formal analysis, Visualization, Methodology, Writing – original draft, Writing – review and editing. P.T.: Supervision, Funding acquisition, Writing – review and editing. K.A.B.: Investigation, Resources, Data Curation, Writing – review and editing. A.B.L.T.: Supervision, Funding acquisition, Project administration, Writing – review and editing.

DECLARATION OF INTERESTS

The authors declare no competing interests.

STAR★METHODS

Detailed methods are provided in the online version of this paper and include the following:

SUPPLEMENTAL INFORMATION

Supplemental information can be found online at https://doi.org/10.1016/j.isci.2024.111275.

Received: June 7, 2024
Revised: August 8, 2024
Accepted: October 25, 2024
Published: October 28, 2024

REFERENCES

1. Varela, F., Lachaux, J.P., Rodriguez, E., and Martinerie, J. (2001). The brainweb: phase synchronization and large-scale integration. Nat. Rev. Neurosci. *2*, 229–239.
2. Han, Y., Kebschull, J.M., Campbell, R.A.A., Cowan, D., Imhof, F., Zador, A.M., and Mrsic-Flogel, T.D. (2018). The logic of single-cell projections from visual cortex. Nature *556*, 51–56.
3. Bressler, S.L. (1995). Large-scale cortical networks and cognition. Brain Res. Brain Res. Rev. *20*, 288–304.
4. Binzegger, T., Douglas, R.J., and Martin, K.A.C. (2004). A quantitative map of the circuit of cat primary visual cortex. J. Neurosci. *24*, 8441–8453.
5. Gupta, A., Wang, Y., and Markram, H. (2000). Organizing principles for a diversity of

GABAergic interneurons and synapses in the neocortex. Science *287*, 273–278.
6. Felleman, D.J., and Van Essen, D.C. (1991). Distributed Hierarchical Processing in the Primate Cerebral Cortex. Cerebr. Cortex *1*, 1–47.
7. Bugeon, S., Duffield, J., Dipoppa, M., Ritoux, A., Prankerd, I., Nicoloutsopoulos, D., Orme, D., Shinn, M., Peng, H., Forrest, H., et al. (2022). A transcriptomic axis predicts state modulation of cortical interneurons. Nature *607*, 330–338.
8. Bastos, A.M., Vezoli, J., Bosman, C.A., Schoffelen, J.-M., Oostenveld, R., Dowdall, J.R., De Weerd, P., Kennedy, H., and Fries, P. (2015). Visual areas exert feedforward and feedback influences through distinct frequency channels. Neuron *85*, 390–401. https://doi.org/10.1101/004804.
9. Kohn, A., Jasper, A.I., Semedo, J.D., Gokcen, E., Machens, C.K., and Yu, B.M. (2020). Principles of Corticocortical Communication: Proposed Schemes and Design Considerations. Trends Neurosci. *43*, 725–737.
10. Ebitz, R.B., and Hayden, B.Y. (2021). The population doctrine in cognitive neuroscience. Neuron *109*, 3055–3068.
11. Semedo, J.D., Zandvakili, A., Machens, C.K., Yu, B.M., and Kohn, A. (2019). Cortical Areas Interact through a Communication Subspace. Neuron *102*, 249–259.e4.
12. Semedo, J.D., Jasper, A.I., Zandvakili, A., Krishna, A., Aschner, A., Machens, C.K., Kohn, A., and Yu, B.M. (2022). Feedforward and feedback interactions between visual cortical areas use different population activity patterns. Nat. Commun. *13*, 1099.
13. Veuthey, T.L., Derosier, K., Kondapavulur, S., and Ganguly, K. (2020). Single-trial cross-area neural population dynamics during long-term skill learning. Nat. Commun. *11*, 4057.
14. Kim, J., Joshi, A., Frank, L., and Ganguly, K. (2023). Cortical-hippocampal coupling during manifold exploration in motor cortex. Nature *613*, 103–110.
15. Kaufman, M.T., Churchland, M.M., Ryu, S.I., and Shenoy, K.V. (2014). Cortical activity in the null space: permitting preparation without movement. Nat. Neurosci. *17*, 440–448.
16. MacDowell, C.J., Libby, A., Jahn, C.I., Tafazoli, S., and Buschman, T.J. (2023). Multiplexed Subspaces Route Neural Activity Across Brain-wide Networks. Preprint at bioRxiv. https://doi.org/10.1101/2023.02.08.527772.
17. Tafazoli, S., Bouchacourt, F.M., Ardalan, A., Markov, N.T., Uchimura, M., Mattar, M.G., Daw, N.D., and Buschman, T.J. (2024). Building compositional tasks with shared neural subspaces. Preprint at bioRxiv. https://doi.org/10.1101/2024.01.31.578263.
18. Semedo, J.D., Gokcen, E., Machens, C.K., Kohn, A., and Yu, B.M. (2020). Statistical methods for dissecting interactions between brain areas. Curr. Opin. Neurobiol. *65*, 59–69.
19. Chae, H., Banerjee, A., Dussauze, M., and Albeanu, D.F. (2022). Long-range functional loops in the mouse olfactory system and their roles in computing odor identity. Neuron *110*, 3970–3985.e7.
20. Chen, Y., Chen, X., Baserdem, B., Zhan, H., Li, Y., Davis, M.B., Kebschull, J.M., Zador, A.M., Koulakov, A.A., and Albeanu, D.F. (2022). High-throughput sequencing of single neuron projections reveals spatial organization in the olfactory cortex. Cell *185*, 4117–4134.e28.
21. Otazu, G.H., Chae, H., Davis, M.B., and Albeanu, D.F. (2015). Cortical Feedback Decorrelates Olfactory Bulb Output in Awake Mice. Neuron *86*, 1461–1477.
22. Bolding, K.A., and Franks, K.M. (2018). Recurrent cortical circuits implement concentration-invariant odor coding. Science *361*, eaat6904. https://doi.org/10.1126/science.aat6904.
23. Bolding, K.A., and Franks, K.M. (2017). Complementary codes for odor identity and intensity in olfactory cortex. Elife *6*, e22630. https://doi.org/10.7554/eLife.22630.
24. Pashkovski, S.L., Iurilli, G., Brann, D., Chicharro, D., Drummey, K., Franks, K.M., Panzeri, S., and Datta, S.R. (2020). Structure and flexibility in cortical representations of odour space. Nature *583*, 253–258.
25. Blazing, R.M., and Franks, K.M. (2020). Odor coding in piriform cortex: mechanistic insights into distributed coding. Curr. Opin. Neurobiol. *64*, 96–102.
26. Gonzalez, J., Torterolo, P., and Tort, A.B.L. (2023). Mechanisms and functions of respiration-driven gamma oscillations in the primary olfactory cortex. Elife *12*, e83044. https://doi.org/10.7554/eLife.83044.
27. González, J., Cavelli, M., Mondino, A., Castro-Zaballa, S., Brankačk, J., Draguhn, A., Torterolo, P., and Tort, A.B.L. (2023). Breathing modulates gamma synchronization across species. Pflügers Archiv *475*, 49–63.
28. Spors, H., Albeanu, D.F., Murthy, V.N., Rinberg, D., Uchida, N., Wachowiak, M., and Friedrich, R.W. (2012). Illuminating vertebrate olfactory processing. J. Neurosci. *32*, 14102–14108.
29. Dhawale, A.K., Hagiwara, A., Bhalla, U.S., Murthy, V.N., and Albeanu, D.F. (2010). Non-redundant odor coding by sister mitral cells revealed by light addressable glomeruli in the mouse. Nat. Neurosci. *13*, 1404–1412.
30. Wachowiak, M. (2011). All in a sniff: olfaction as a model for active sensing. Neuron *71*, 962–973.
31. Abraham, N.M., Spors, H., Carleton, A., Margrie, T.W., Kuner, T., and Schaefer, A.T. (2004). Maintaining accuracy at the expense of speed: stimulus similarity defines odor discrimination time in mice. Neuron *44*, 865–876.
32. Smear, M., Shusterman, R., O'Connor, R., Bozza, T., and Rinberg, D. (2011). Perception of sniff phase in mouse olfaction. Nature *479*, 397–400.
33. Tort, A.B.L., Brankačk, J., and Draguhn, A. (2018). Respiration-Entrained Brain Rhythms Are Global but Often Overlooked. Trends Neurosci. *41*, 186–197.
34. Kluger, D.S., Balestrieri, E., Busch, N.A., and Gross, J. (2021). Respiration aligns perception with neural excitability. Elife *10*, e70907. https://doi.org/10.7554/eLife.70907.
35. Perl, O., Ravia, A., Rubinson, M., Eisen, A., Soroka, T., Mor, N., Secundo, L., and Sobel, N. (2019). Human non-olfactory cognition phase-locked with inhalation. Nat. Human Behav. *3*, 501–512.
36. Yackle, K., Schwarz, L.A., Kam, K., Sorokin, J.M., Huguenard, J.R., Feldman, J.L., Luo, L., and Krasnow, M.A. (2017). Breathing control center neurons that promote arousal in mice. Science *355*, 1411–1415.
37. Del Negro, C.A., Funk, G.D., and Feldman, J.L. (2018). Breathing matters. Nat. Rev. Neurosci. *19*, 351–367.
38. Lockmann, A.L.V., Laplagne, D.A., Leão, R.N., and Tort, A.B.L. (2016). A Respiration-Coupled Rhythm in the Rat Hippocampus Independent of Theta and Slow Oscillations. J. Neurosci. *36*, 5338–5352.
39. Bagur, S., Lefort, J.M., Lacroix, M.M., de Lavilléon, G., Herry, C., Chouvaeff, M., Billand, C., Geoffroy, H., and Benchenane, K. (2021). Breathing-driven prefrontal oscillations regulate maintenance of conditioned-fear evoked freezing independently of initiation. Nat. Commun. *12*, 2605.
40. Ito, J., Roy, S., Liu, Y., Cao, Y., Fletcher, M., Lu, L., Boughter, J.D., Grün, S., and Heck, D.H. (2014). Whisker barrel cortex delta oscillations and gamma power in the awake mouse are linked to respiration. Nat. Commun. *5*, 3572.
41. Zelano, C., Jiang, H., Zhou, G., Arora, N., Schuele, S., Rosenow, J., and Gottfried, J.A. (2016). Nasal Respiration Entrains Human Limbic Oscillations and Modulates Cognitive Function. J. Neurosci. *36*, 12448–12467.
42. Shusterman, R., Smear, M.C., Koulakov, A.A., and Rinberg, D. (2011). Precise olfactory responses tile the sniff cycle. Nat. Neurosci. *14*, 1039–1044.
43. Franks, K.M., and Isaacson, J.S. (2006). Strong single-fiber sensory inputs to olfactory cortex: implications for olfactory coding. Neuron *49*, 357–363.
44. Stern, M., Bolding, K.A., Abbott, L.F., and Franks, K.M. (2018). A transformation from temporal to ensemble coding in a model of piriform cortex. Elife *7*, e34831. https://doi.org/10.7554/eLife.34831.
45. Wilson, C.D., Serrano, G.O., Koulakov, A.A., and Rinberg, D. (2017). A primacy code for odor identity. Nat. Commun. *8*, 1477.
46. Mombaerts, P., Wang, F., Dulac, C., Chao, S.K., Nemes, A., Mendelsohn, M., Edmondson, J., and Axel, R. (1996). Visualizing an olfactory sensory map. Cell *87*, 675–686.
47. Soucy, E.R., Albeanu, D.F., Fantana, A.L., Murthy, V.N., and Meister, M. (2009). Precision and diversity in an odor map on the olfactory bulb. Nat. Neurosci. *12*, 210–220.
48. Sosulski, D.L., Bloom, M.L., Cutforth, T., Axel, R., and Datta, S.R. (2011). Distinct representations of olfactory information in different cortical centres. Nature *472*, 213–216.
49. Ghosh, S., Larson, S.D., Hefzi, H., Marnoy, Z., Cutforth, T., Dokka, K., and Baldwin, K.K. (2011). Sensory maps in the olfactory cortex defined by long-range viral tracing of single neurons. Nature *472*, 217–220.
50. Miyamichi, K., Amat, F., Moussavi, F., Wang, C., Wickersham, I., Wall, N.R., Taniguchi, H., Tasic, B., Huang, Z.J., He, Z., et al. (2011). Cortical representations of olfactory input by trans-synaptic tracing. Nature *472*, 191–196.
51. Igarashi, K.M., Ieki, N., An, M., Yamaguchi, Y., Nagayama, S., Kobayakawa, K., Kobayakawa, R., Tanifuji, M., Sakano, H., Chen, W.R., and Mori, K. (2012). Parallel mitral and tufted cell pathways route distinct odor information to different targets in the olfactory cortex. J. Neurosci. *32*, 7970–7985.
52. Stettler, D.D., and Axel, R. (2009). Representations of odor in the piriform cortex. Neuron *63*, 854–864.
53. Rennaker, R.L., Chen, C.-F.F., Ruyle, A.M., Sloan, A.M., and Wilson, D.A. (2007). Spatial and temporal distribution of odorant-evoked activity in the piriform cortex. J. Neurosci. *27*, 1534–1542.
54. Poo, C., and Isaacson, J.S. (2009). Odor Representations in Olfactory Cortex: "Sparse" Coding, Global Inhibition, and Oscillations. Neuron *62*, 850–861.

55. Karalis, N., Dejean, C., Chaudun, F., Khoder, S., Rozeske, R.R., Wurtz, H., Bagur, S., Benchenane, K., Sirota, A., Courtin, J., and Herry, C. (2016). 4-Hz oscillations synchronize prefrontal–amygdala circuits during fear behavior. Nat. Neurosci. *19*, 605–612.
56. Kluger, D.S., and Gross, J. (2021). Respiration modulates oscillatory neural network activity at rest. PLoS Biol. *19*, e3001457.
57. Juventin, M., Ghibaudo, V., Granget, J., Amat, C., Courtiol, E., and Buonviso, N. (2023). Respiratory influence on brain dynamics: the preponderant role of the nasal pathway and deep slow regime. Pflügers Archiv *475*, 23–35. https://doi.org/10.1007/s00424-022-02722-7.
58. Yanovsky, Y., Ciatipis, M., Draguhn, A., Tort, A.B.L., and Brankačk, J. (2014). Slow oscillations in the mouse hippocampus entrained by nasal respiration. J. Neurosci. *34*, 5949–5964.
59. Tort, A.B.L., Hammer, M., Zhang, J., Brankačk, J., and Draguhn, A. (2021). Temporal Relations between Cortical Network Oscillations and Breathing Frequency during REM Sleep. J. Neurosci. *41*, 5229–5242.
60. Karalis, N., and Sirota, A. (2022). Breathing coordinates cortico-hippocampal dynamics in mice during offline states. Nat. Commun. *13*, 467.
61. Salinas, E., and Sejnowski, T.J. (2001). Correlated neuronal activity and the flow of neural information. Nat. Rev. Neurosci. *2*, 539–550.
62. Kumar, A., Rotter, S., and Aertsen, A. (2010). Spiking activity propagation in neuronal networks: reconciling different perspectives on neural coding. Nat. Rev. Neurosci. *11*, 615–627.
63. Churchland, M.M., and Shenoy, K.V. (2024). Preparatory activity and the expansive null-space. Nat. Rev. Neurosci. *25*, 213–236.
64. Esquivelzeta Rabell, J., Mutlu, K., Noutel, J., Martin Del Olmo, P., and Haesler, S. (2017). Spontaneous Rapid Odor Source Localization Behavior Requires Interhemispheric Communication. Curr. Biol. *27*, 1542–1548.e4.
65. Wagner, M.J., and Smith, M.A. (2008). Shared internal models for feedforward and feedback control. J. Neurosci. *28*, 10663–10673.
66. Srinivasan, S., Daste, S., Modi, M.N., Turner, G.C., Fleischmann, A., and Navlakha, S. (2023). Effects of stochastic coding on olfactory discrimination in flies and mice. PLoS Biol. *21*, e3002206.
67. Bolding, K.A., and Franks, K.M. (2023). Electrophysiological Recordings from Identified Cell Types in the Olfactory Cortex of Awake Mice. Methods Mol. Biol. *2710*, 209–221.
68. Tantirigama, M.L.S., Huang, H.H.-Y., and Bekkers, J.M. (2017). Spontaneous activity in the piriform cortex extends the dynamic range of cortical odor coding. Proc. Natl. Acad. Sci. USA *114*, 2407–2412.
69. Sirotin, Y.B., Shusterman, R., and Rinberg, D. (2015). Neural Coding of Perceived Odor Intensity. eNeuro *2*, ENEURO.0083-15.2015. https://doi.org/10.1523/ENEURO.0083-15.2015.

STAR★METHODS

KEY RESOURCES TABLE

REAGENT or RESOURCE	SOURCE	IDENTIFIER
Deposited data		
pcx-1 dataset	http://crcns.org	https://doi.org/10.6080/K00C4SZB
Software and algorithms		
CS_OB-PCx	https://github.com/ https://zenodo.org/	https://github.com/joaqgonzar/CS_OB-PCx https://doi.org/10.5281/zenodo.13755624

EXPERIMENTAL MODEL AND STUDY PARTICIPANT DETAILS

Animals

We analyzed simultaneous OB and PCx recordings generously made available by Bolding and Franks through the Collaborative Research in Computational Neuroscience data-sharing website (http://crcns.org, pcx-1 dataset). The SIMUL and TeLC-THY experiments were employed. Detailed descriptions of the experimental procedures are found in previous publications.[22,23,67] The Institutional Animal Care and Use Committee of Duke University approved all protocols according to protocols A243-12-09 and A220-15-08. Below we describe the analytical methods employed and the relevant experimental procedures from the original publication.

Female and male adult mice were employed (>P60, 20–24 g); animals were housed in single cages on a normal light-dark cycle (n = 12 mice). For the optogenetic experiments, the mice employed were adult Thy1ChR2/ChR2-YFP, line 18 (Thy1-COP4/EYFP, Jackson Laboratory, 007612, n = 5 mice). For the combined optogenetics and TeLC expression experiments, adult offspring of Emx1Cre/Cre mice crossed with Thy1ChR2/ChR2-YFP mice were employed (n = 7 mice).

METHOD DETAILS

Adeno-associated viral vectors

For the TeLC experiments, AAV5-DIO-TeLC-GFP was expressed under CBA control (6/7 mice) or synapsin (1/7 mice); since effects were similar in either, data were pooled together. Three 500 nL injections in the PCx (AP, ML, DV: +1.8, 2.7, 3.85; +0.5, 3.5, 3.8; −1.5, 3.9, 4.2 mm; DV measured from brain surface) were employed to achieve TeLC expression. All recordings took place ∼14 days after the promoter injection. All viruses were obtained from the University of North Carolina-Chapel Hill (UNC Vector Core).

Data acquisition

The electrophysiological signals were recorded through 32-site polytrode acute probes (A1x32-Poly3-5mm- 25 s-177, Neuronexus) with an A32-OM32 adaptor (Neuronexus) through a Cereplex digital headstage (Blackrock Microsystems). Data were acquired at 30 kHz, unfiltered, employing a Cerebus multichannel data acquisition system (BlackRock Microsystems). Respiration was acquired at 2 kHz by analog inputs of the Cerebus system. The respiration signal was measured employing a microbridge mass airflow sensor (Honeywell AWM3300V), which was positioned opposite to the animal's nose. Inhalation generated a negative airflow and thus negative changes in the voltage of the sensor output.

Electrode and optic fiber placement

For OB recordings, a Patchstar Micromanipulator (Scientifica) holding the silicon probe was set to a 10-degree angle in the coronal plane to target the ventrolateral mitral cell layer. The probe was first positioned above the OB center (4.85 mm AP, 0.6 mm ML from bregma) and then lowered following this angle until dense spiking activity was found from the mitral cell layer, typically between 1.5 and 2.5 mm from the OB surface. For PCx recordings, the micromanipulator was employed to position the recording probe in the anterior PCx (1.32 mm AP and 3.8 mm ML). Recordings were targeted 3.5–4 mm ventral from the brain surface at this position and were further adjusted according to the LFP and spiking activity monitored online. The electrode sites spanned 275 μm along the dorsal-ventral axis. The probe was lowered until an intense spiking band was found, which covered 30–40% of electrode sites near the correct ventral coordinate, thus reflecting the piriform layer II. For the optogenetic experiments stimulating OB cells in Thy1ChR2/ChR2-YFP mice, the optic fiber was placed <500 μm above the OB dorsal surface.

Spike sorting and waveform characteristics

Spyking-Circus software was employed to isolate individual units (https://github.com/spyking-circus). All clusters which had more than 1% of ISIs violating the refractory period (<2 ms) or appearing contaminated were manually removed. Units that showed similar waveforms and

coordinated refractory periods were merged into single clusters. The number of single cells simultaneously recorded per area during each session is shown in Table S1. Figures S12A and S12B shows all refractory period violations and the average waveform amplitudes for each isolated single unit. The reader is referred to ref.[23] for representative isolation distance results of putative single cells (5/13 simultaneous OB/PCx recordings).

Odor delivery

Stimuli consisted of monomolecular odorants diluted in mineral oil. The odorants employed were: hexanal, ethyl butyrate, ethyl acetate, 2-hexanone, isoamyl acetate, and ethyl tiglate. Odor stimuli were presented for 1 s through an olfactometer controlled by MATLAB scripts and repeated every 10 s. Average firing rates during spontaneous activity and the whole period of odor deliveries are shown in Figure S12C. Note that average firing rates did not change in the OB during odor presentations and slightly decreased in the PCx, consistent with ref.[68,69] For single cell responses to different odorants, the reader is referred to ref.[22,23]

Anesthesia recordings

In 11 out of 13 mice, a combination of ketamine and xylazine at a dose of 100/10 mg/kg was injected intraperitoneally, leading to consistent anesthesia for 30–45 min. Body temperature was regulated using a heating pad throughout this period. The initial 30 min after the onset of slow oscillation were utilized for all assessments. One mouse was excluded from the analysis due to the absence of any physiological indications of anesthesia.

QUANTIFICATION AND STATISTICAL ANALYSIS

For all analyses, we used Python 3 with numpy (https://numpy.org/), scipy (https://docs.scipy.org/), matplotlib (https://matplotlib.org/), sklearn (https://scikit-learn.org/stable/), and pyinform (https://elife-asu.github.io/PyInform/).

INDIVIDUAL CELL SPIKING PREPROCESSING

The spike times were rounded to match the respiration signal resolution (0.5 ms or 2000 Hz sampling rate). Then, we convolved the spike times of each unit with a 10 ms standard deviation Gaussian kernel employing the convolve scipy function (in close similarity with the original publication), which gave rise to a smoothed spiking activity. To obtain the MUA signals, we summed the smoothed firing rate of each individual neuron within a population, obtaining a 1-d signal.

CANONICAL CORRELATION ANALYSIS TO STUDY THE COMMUNICATION SUBSPACE

Before performing canonical correlation analysis (CCA), all smoothed spike trains were z-scored by subtracting the mean firing rate and dividing the result by the standard deviation. CCA seeks to find the sets of weights Wx and Wy that maximize the Pearson correlation coefficient between the X and Y vectors (when weighted by Wx and Wy). In our case, X and Y correspond to the smoothed firing rates of two different neuronal populations. CCA is thus defined by:

$$W_x, W_y = argmax_{Wx,Wy}\left[\rho\left(W_xX, W_yY\right)\right]$$

where:

$$\rho\left(W_xX, W_yY\right) = \frac{COV\left(W_xX, W_yY\right)}{\sqrt{VAR(\ W_xX)\ VAR\left(W_yY\right)}}$$

$COV()$ and $VAR()$ being the covariance and variance respectively.

Wx and Wy are the weight vectors that point-by-point multiply X and Y activity (i.e., $W_x\ X = W_{x1}\ x1 + W_{x2}\ x2 + \ldots + W_{xN}\ xN$). They are related to the X and Y firing vectors through their Σxy covariance matrix:

$$\rho^2 Wy = \left(\Sigma yy^{-1}\ \Sigma yx\ \Sigma xx^{-1}\ \Sigma xy\right)\ Wy$$

$$\rho^2 Wx = \left(\Sigma xx^{-1}\ \Sigma xy\ \Sigma yy^{-1}\ \Sigma yx\right)\ Wx$$

We can see that the above equation is in the form of the standard eigenvalue problem $Av = \lambda v$, where $\lambda = \rho^2$ is the eigenvalue of the $A = \Sigma yy^{-1}\ \Sigma yx\ \Sigma xx^{-1}\ \Sigma xy$ matrix, and $Wy = v$ is the corresponding eigenvector. Thus, the Wy and Wx vectors are found as the eigenvectors of the $\Sigma yy^{-1}\ \Sigma yx\ \Sigma xx^{-1}\ \Sigma xy$ and $\Sigma xx^{-1}\ \Sigma xy\ \Sigma yy^{-1}\ \Sigma yx$ modified covariance matrices respectively.

Note that there exist M Wy and Wx vectors that satisfy the previous equations, which are all the eigenvectors of the above mentioned covariance matrices, where $= min(Nx, Ny)$, that is, the minimum number of neurons in either the X or Y population. Each M vector pair defines one communication subspace (CS) pair. These pairs are ordered according to the correlation coefficient (R) they produce, i.e., $R(CS_1) > R(CS_2) > R(CS_3) > \ldots > R(CS_M)$. Of note, because each CS pair is one of the eigenvectors of the modified covariance matrix, they are orthogonal against each other, implying that the different CS dimensions for a given area are not correlated.

For the practical implementation, we employed the *CCA* sklearn function employing *max_iter=100000, tol = 1e-12*. The weights were obtained through the *x_weights_* and *y_weights_* methods of the *CCA* object. The CS activity was obtained through the *fit.transform CCA* method. CS and MUA signals were z-scored to allow comparisons.

Time-lagged CCA

The correlation between CS activities was computed using the Pearson correlation coefficient *pearsonr* stats.scipy function. To find the optimal lag between both OB and PCx CS signals, we temporally lagged PCx activity by different times and computed CCA to find the time-lag which maximizes the OB-PCx CS correlation. The weights obtained for this time-maximizing correlations were employed subsequently to obtain the respective CS signals.

Surrogate analysis

To understand how many significant CS pairs exist, we contrasted CS correlations through a surrogate analysis. To generate a surrogate distribution to compare CS correlation values, we circularly shifted the spiking activity of one of the populations in time by random amounts. For each surrogate data, we computed the CCA and obtained the correlation coefficient for the first most correlated pair (CS_1). The procedure was repeated 100 times for each session, and all surrogate correlation coefficients were pooled together to yield an $N = 1300$ surrogate distribution (100 surrogates from 13 sessions across 12 animals). We then assessed the significance by comparing the correlation coefficient for each CS pair against the null surrogate distribution. Only correlation values above the 99th percentile were deemed significant ($p < 0.01$).

Cross-correlation analysis

Cross-correlations between OB-PCx CS signals or MUA signals were estimated employing the *correlate* signal.scipy function using the *mode='same'* and *method='fft'* parameters.

Directionality analysis

We calculated the transfer entropy between the binarized CS_1 signals to study the directionality between OB and PCx CS_1 signals. The binarization procedure assigned a 0 when the CS_1 signal was below the mean CS_1 or a 1 when the CS_1 signal was above the mean. Then, transfer entropy was estimated using a 10 ms history length between signals.

Specifically, transfer entropy is defined as:

$$TE_{X\rightarrow Y} = H(Y \,/\, Y_{t-1:t-l}) - H(Y \,/\, Y_{t-1:t-l}, X_{t-1:t-l})$$

where $H(Y \,/\, Y_{t-1:t-l})$ is the conditional Shannon entropy of the Y signal given its previous history. $l = 10$ ms in our analysis (20 time points).

The same analysis was employed to study Resp-CS_1 directionality, the only difference being that Resp and CS_1 signals were down-sampled to 40 Hz and $l = 500$ ms in our analysis (20 time points).

Principal component analysis

PCA finds subsets of correlated neurons within each area. The principal components (PCs) are found through the eigenvectors (v) of the covariance matrix (Σxx), $\Sigma xx\ v = \lambda v$, where λ are the eigenvalues (explained variance of that PC) of Σxx. We employed the *PCA* sklearn function to compute the PCs of the OB and PCx activity (the same OB and PCx activity vectors employed for CCA were used for PCA).

Power spectrum and coherence

We computed Welch's modified periodogram to estimate the CS spectra (*welch* scipy function). Specifically, we employed a 1 s moving window with half a window overlap, setting the numerical frequency resolution to 0.1 Hz (by setting the nfft parameter to 10 times the sampling rate). Similarly, we computed the magnitude squared coherence (OB-Resp, PCx-Resp, OB-PCx) through the *coherence* scipy function employing the abovementioned parameters.

To obtain a surrogate CS-Resp coherence distribution (Figure S4B), we circularly shifted the Resp signal in time by random amounts and repeated the procedure 100 times per session. Individual CS-Resp coherence values were then compared against the null distribution (made from CS_1- shuffled Resp coherence), and only the values above the 99th percentile were considered significant ($p < 0.01$).

Spike-phase, correlation-phase, and directionality-phase plots

We computed the average spiking activity per respiration phase by first band-pass filtering the respiration signal using the *eegfilt* function adapted for Python 3 (available at https://github.com/joaqgonzar/Gamma_Oscillations_PCx). We filtered the signal between 1 and 3 Hz to obtain the slower frequency component. The phase (angle) of the filtered respiration signal was estimated from their analytical representation based on the Hilbert transform. We then binned the phase time series into 300 bins and computed the mean spiking activity of each neuron for each respiration phase bin. Similarly, for each respiration phase bin, the correlation between the OB CS_1 and PCx CS_1 was computed using only the time points associated to it. For the directionality-phase plot, we computed transfer entropy for each phase bin employing a history length of 10 ms (see transfer entropy details above).

Spike-spike histogram

For each recording session, we measured spike-spike histograms between OB and PCx neurons. We first selected the ten most positive OB neurons according to their CS_1 weights and the ten most positive and negative CS_1-weighted PCx neurons. We constructed histograms (employing 10 ms bins) of the time differences between an OB neuron spike and the spikes of a PCx neuron. To compare the shape of the histograms (Figure 4D), we z-scored them by subtracting the mean and dividing them by the standard deviation. Peak activity (excitation/inhibition) shown in Figure 4E was obtained by selecting from each normalized histogram the time lag that had the largest positive (excitation) or negative (inhibition) value.

Odor decoding from CS activity

We employed a supervised linear classifier to decode either odor identity (six different odorants at 0.3% v./v. concentration) or odor concentration (four concentrations from 2 different odorants) from the CS activity. We supplied the average CS activity (CS_1, [CS_1,CS_2], [CS_1,CS_2,CS_3] etc.) during the first 500 ms following the inhalation start. The classification algorithm was a linear support vector machine with a stochastic gradient descent optimization, implemented using the *sgdclassifier* sklearn function. Each session was trained and tested separately using leave-one-out cross-validation through the *LeaveOneOut* sklearn function; for each iteration, a single odor trial was withheld from training and tested later; the procedure was repeated for all odor trials, and the mean accuracy was reported.

Odor cluster distances were computed by first calculating the center of mass of each cluster and then computing the Euclidean distance between the center of mass of 2 clusters. Surrogate distributions were obtained by shuffling odor labels and computing the distance of the surrogate clusters. This procedure was repeated 500 times for each animal.

Toy model for studying cross-area communication

We employed two different strategies to construct a toy model to validate CCA.

1) We generated two 10 × 10000 random firing rate matrices (X and Y areas in Figure S1), representing ten neurons in each area and 10000 time points. On top of that, we imposed several activation times (specific moments in time when firing rates increased substantially). These activation times could be either local (occurring in only one matrix) or shared between both matrices (Figures S1A and S1B). To study lagged communication (Figure S3), we made the common activation times (shared between both matrices) to be lagged in time by two time points. To overcome the fact that CCA cannot deal with lagged correlations, we either convolved the matrices with a Gaussian kernel or lagged one of the two matrices in time before performing CCA.
2) We also tested a synthetic case in which a set of Y neurons would receive a linear combination of X outputs (without any common activation times). In the example of Figure S1C,

$$Y1 = -0.24X1 + 0.7X2 + 0.68X3$$

$$Y5 = 0.96X4 + 0.09X5 + 0.25X6$$

$$Y9 = -0.12X7 - 0.71X8 + 0.69X9$$

Where Y1 stands for neuron 1 of the Y area and so on. The weights of the combinations were picked to be orthogonal vectors to make the different combinations independent. For Figure S1D, we increased the number of independent combinations from 0 to 10 and measured the correlations obtained from each CS activity pair.

Statistics

We show group data as either mean ± SEM or regular boxplots showing the median, 1st, 3rd quartiles, and the distribution range without outliers. We employed paired one-sided (Figure 7B) and two-sided paired t-test (all remaining results except 5C and 7E) to compare between groups. For Figures 5C and 7E we employed two-way ANOVAs. We additionally employed a one-sample one-sided t-test to compare decoding accuracies against chance levels. We set $p < 0.05$ to be considered significant (in the figure panels, *, ** and *** denote $p < 0.05$, $p < 0.01$, and $p < 0.001$, respectively). Figure panels (and main text) provide the statistical tests used, exact value of n, what n represents, definition of center, dispersion, and precision measures.